## Majority of global river flow sustained by groundwater

Xie, Jiaxin; Liu, Xiaomang; Jasechko, Scott; Berghuijs, Wouter R.; Wang, Kaiwen; Liu, Changming; Reichstein, Markus; Jung, Martin; Koirala, Sujan

***published in***
Nature Geoscience
2024

***DOI (link to publisher)***
10.1038/s41561-024-01483-5

***document version***
Publisher's PDF, also known as Version of record

nature geoscience

Article

https://doi.org/10.1038/s41561-024-01483-5

# Majority of global river flow sustained by groundwater

Received: 4 November 2023

Accepted: 14 June 2024

Published online: 19 July 2024

Check for updates

Jiaxin Xie[1,2,6], Xiaomang Liu[1] ✉, Scott Jasechko[3], Wouter R. Berghuijs[4], Kaiwen Wang[1], Changming Liu[1], Markus Reichstein[5,6], Martin Jung[6] & Sujan Koirala[6]

Groundwater-sustained baseflow is a vital source of river flow, especially during dry seasons. The proportion of river flow sustained by baseflow—the baseflow index—is essential for assessing fluvial nutrient cycling and contaminant transport. However, the global baseflow index remains highly uncertain, with current Earth system model simulations ranging from 12% to 94%. Here we estimate the global baseflow index to be 59% ± 7% based on an emergent constraint approach, which integrates 50 Earth system models with baseflow indices derived from streamflow observations in 15,567 basins. Our observational constraint indicates that at least 21% ± 3% of precipitation recharges groundwater, which is approximately double the figure reported in the Sixth Assessment Report of the United Nations Intergovernmental Panel on Climate Change. Thus, our research suggests a more active role of groundwater in the global water cycle than most Earth system models currently simulate. We present evidence that the considerable disagreement in simulated baseflow stems from unrealistic and varied model representations of infiltration, aquifer structure and groundwater dynamics. These processes should be prioritized so that models can capture active groundwater–river connections.

Groundwater is an actively flowing component of the hydrological cycle, and its discharge into rivers provides an important source of streamflow in rivers around the globe[1,2]. The water table—the depth below which pore spaces are water saturated—splits streamflow generation into two parts. In the upper part (above the water table), water may flow to streams as either overland flow or subsurface stormflow, which bypasses the water table and typically occurs during or shortly after rainfall[3]. In the lower part (groundwater flow beneath the water table), water percolates past the unsaturated zone to the water table to recharge groundwater, and some of this groundwater may flow downgradient to discharge into streams, generating 'baseflow' in streams[4,5].

This baseflow serves as a reliable water source to rivers, sustaining perennial flows and thus playing a vital role in surface water supply and ecosystem services. For example, baseflow can regulate water temperatures during droughts and provide continuous habitat for aquatic organisms[6]. Assessing the proportion of long-term baseflow to streamflow—the 'baseflow index'—can help characterize groundwater–surface water connections and concomitant consequences, such as fluvial nutrient cycling[7], contaminant transport[8], chemical weathering[9] and the role of groundwater in shaping floods[10], meaning that it is important for models to adequately simulate baseflow if these projections are to be used to project flood risk and water availability[11].

[1]Key Laboratory of Water Cycle and Related Land Surface Processes, Institute of Geographic Sciences and Natural Resources Research, Chinese Academy of Sciences, Beijing, China. [2]University of Chinese Academy of Sciences, Beijing, China. [3]Bren School of Environmental Science and Management, University of California, Santa Barbara, CA, USA. [4]Department of Earth Sciences, Free University Amsterdam, Amsterdam, Netherlands. [5]ELLIS Unit Jena, Jena, Germany. [6]Present address: Department of Biogeochemical Integration, Max Planck Institute for Biogeochemistry, Jena, Germany. ✉e-mail: liuxm@igsnrr.ac.cn

Despite considerable research efforts, global baseflow index estimates remain highly uncertain. One study[12] utilized artificial neural networks to extend the baseflow index from 3,394 basins (area < 10,000 km$^2$) to global grids. By averaging these grids using run-off as weights, a global baseflow index of 71% is obtained. The Noah Land Surface Model[13] participating in the Global Land Data Assimilation System Version 2.0 produces a global baseflow index of 86%. By contrast, according to the Intergovernmental Panel on Climate Change (IPCC) Sixth Assessment Report[14], the global baseflow index does not exceed 28%.

Earth system models (ESMs) simulate physical processes involved in baseflow generation, such as infiltration and groundwater dynamics, providing an alternative way to estimate the global baseflow index[15]. However, due to their diverse representations of infiltration and groundwater dynamics processes, which have developed along alternative strands over the past few decades, various ESMs inevitably yield divergent baseflow index estimates. Despite the considerable uncertainty in ESMs, they remain the primary tool for assessing future changes in water resources. The wide variability in baseflow index across different ESMs highlights the importance of utilizing real-world measurements to better constrain simulations.

Various methods have been developed to estimate baseflow using measurements, but most are infeasible on a global scale due to a scarcity of adequate data. For example, tracer-based methods use isotopes or chemicals to estimate baseflow, but their global application is limited by laborious and expensive field measurements[11,16,17]. To address this limitation, alternative methods to estimate baseflow indices using streamflow time series have been proposed. For example, a digital filter uses signal analysis to separate baseflow from streamflow, assuming that baseflow is the low-frequency component of streamflow[18,19]. These separation methods have undergone extensive validations in small basins using tracer-based methods as benchmarks[17,20]. Nevertheless, their use in large basins is limited because the underlying assumptions of these methods may not be appropriate for large basins. For example, headwater stormflow of large basins may take weeks to reach the basin outlet and become the low-frequency component of downstream flow. Consequently, these separation methods typically overestimate baseflow in large basins because they misidentify upstream stormflow as baseflow[21]. This limitation is mentioned only in a few studies that set an upper limit of 1,000–10,000 km$^2$ for basin areas when applying these separation methods[12,22–24].

In this Article, we constrain the historical outputs of 50 ESMs under the Coupled Model Intercomparison Project Phase 6 (CMIP6), using baseflow indices calculated from daily streamflow observations in 15,496 small basins (area < 2,500 km$^2$), to derive a new estimate of global baseflow index. Our results provide new constraints on the importance of groundwater in streamflow generation and, thus, surface water availability, demonstrating the importance of improving the realism of ESM simulations of hydrological processes if they are to be used to accurately project water availability.

## Simulated groundwater discharge to rivers

We compiled daily streamflow observations for 48,651 basins (Extended Data Fig. 1), from which 15,496 basins with an area smaller than 2,500 km$^2$ were selected (all areas are within the range of maximum watershed areas for our method to be applicable; see refs. 21–24). We then calculated the baseflow indices for these small basins using 12 baseflow separation methods (see Methods for details). The average baseflow index of the 12 methods served as the observation-based baseflow index, against which the performance of the 50 ESMs was evaluated (Extended Data Table 1). The multimodel mean of the 50 ESMs provides a simulated baseflow index of 52%, which closely aligns with the observation-based mean baseflow index of 55% across the 15,496 basins.

However, we identify substantial differences in the spatial patterns of simulations and observations. Specifically, the multimodel mean tends to overestimate baseflow indices for small basins in the Lower Mississippi River, with values mostly exceeding 50%, whereas the observation-based baseflow indices are predominantly below 30%. For the La Plata River on the east coast of South America, the multimodel mean baseflow indices are less than 40% for most basins, while the observation-based baseflow indices are mostly greater than 70% (Fig. 1a,b). Such divergence in spatial patterns is further highlighted by the mean absolute percentage error of 38% (Fig. 1c), which implies an average bias of 38% between simulated and observation-based baseflow indices across the 15,496 basins.

In addition, large disagreements in simulated baseflow indices across the various models are evidenced in the frequency distribution of Extended Data Fig. 2. For the global baseflow index estimates, the 50 ESMs range from 12% to 94% (the latitudinal distribution in Fig. 1d). For example, MIROC6, CESM2 and ACCESS-ESM1-5 produce global baseflow indices of 12%, 59% and 89%, respectively; the reasons for these large disagreements in simulated baseflow indices are unclear but may include intermodel discrepancies in the parameterization and structure on groundwater-related processes[15].

## Emergent constraint on global baseflow

The wide variability in baseflow indices across ESMs emphasizes the need to use real-world measurements to constrain simulations. Indeed, such constraints have been extensively used to reduce uncertainties in water-flux simulations[25–28]. Yet to the best of our knowledge, no such approach has been applied to test and constrain global baseflow index values using measurements from thousands of drainage basins. Here we use an emergent constraint approach (Methods) to constrain 50 ESM outputs on the basis of observation-based baseflow indices.

The core concept of the emergent constraint approach[25–28] is to discern a relationship shared by multiple ESMs between an observable variable $X$ and an unobservable variable $Y$. In this study, $X$ is the mean baseflow index across the 15,496 basins, and $Y$ is the global baseflow index. We perform regression analysis on the ($X$, $Y$) points of 50 ESMs to identify the shared relationship. The black regression line in Fig. 2a illustrates the strength of this relationship. Substituting an observation of variable $X$ (the observation-based mean baseflow index across basins, denoted by the vertical green line in Fig. 2a) into the relationship, we derive a new global baseflow index of 59%, slightly increasing the multimodel mean of the 50 ESMs (57%). The uncertainty of the new estimate arises mainly from the choice of baseflow separation methods. We used each of the 12 baseflow separation methods to derive 12 constrained baseflow indices. These constrained baseflow indices exhibit a standard variation of 7% (the blue box in Fig. 2a), leading to a 61% reduction in the uncertainty of the 50 ESM ensemble (the yellow box with a standard variation of 18%).

Reference [26] noted that verified mechanisms and out-of-sample testing are required to confirm emergent constraint relationships. The mechanism behind our proposed emergent constraint is that the 15,496 basins well represent baseflow generation patterns across the globe. In other words, for each ungauged basin, we can find gauged basins with similar characteristics that affect baseflow generation, such as climate, topography, landscape and geology. We have collected gauged basins from various sources (Methods), and the 15,496 basins are probably the most representative set currently available, with streamflow records for most basins updated to include data for the past decade (Extended Data Fig. 3). In addition, sensitivity analysis confirms the robustness of the new global baseflow index, even when using only 20% of the 15,496 basins (Extended Data Fig. 4). As for out-of-sample testing, we used two baseflow index datasets based on machine learning[12] and the Noah Land Surface Model[13] as new samples to confirm the emergent constraint relationship. Regarding these two datasets as additional ESMs placed in Fig. 2a, their coordinates will be (0.64, 0.71) and (0.75, 0.86), respectively. Both coordinates are within a 10% deviation of

https://doi.org/10.1038/s41561-024-01483-5

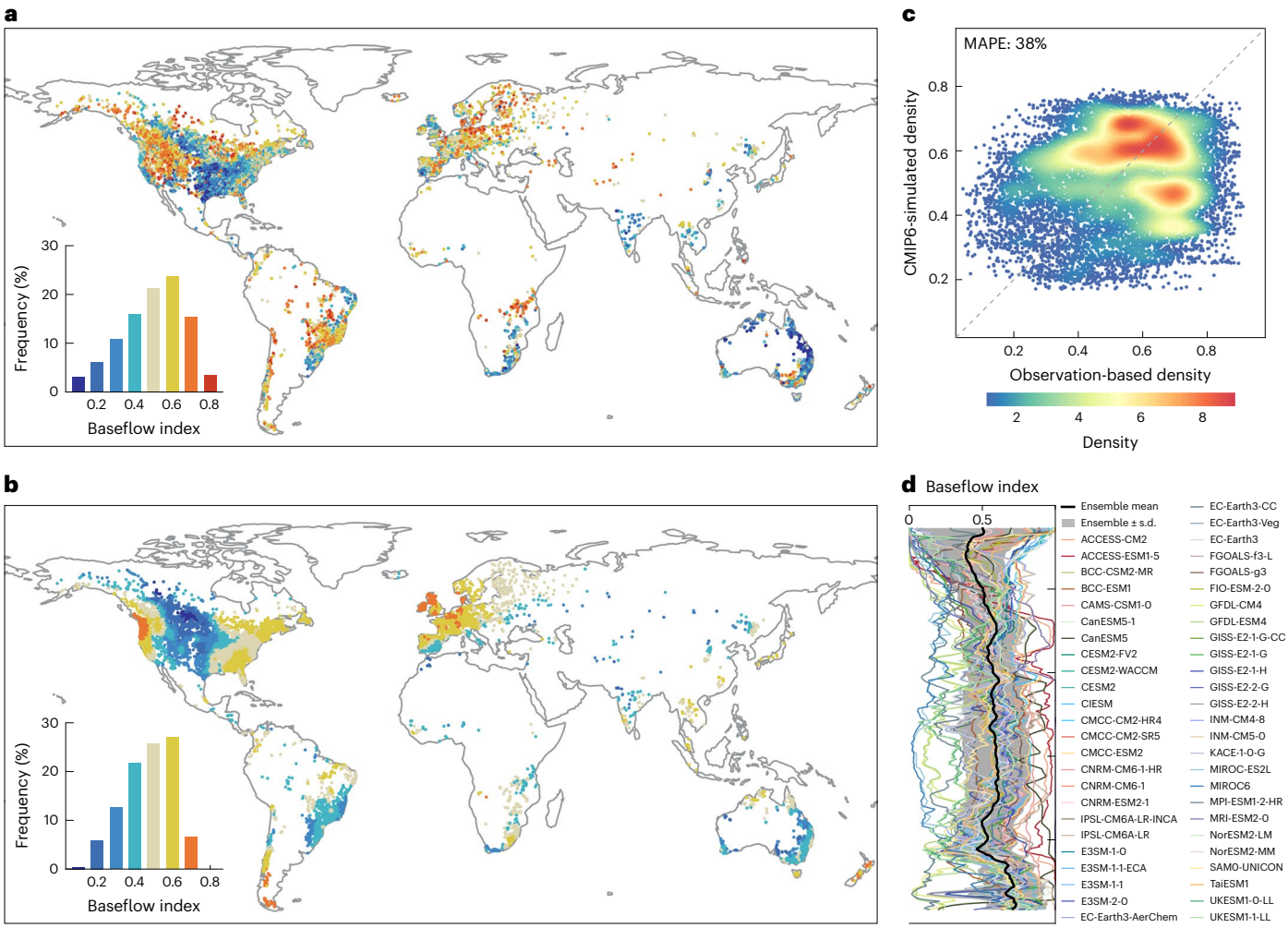


**Fig. 1 | Observation-based and CMIP6-simulated baseflow indices in 15,496 small basins. a**, Baseflow indices calculated from daily streamflow observations using an average of 12 baseflow separation methods. **b**, Multimodel mean baseflow indices derived from 50 CMIP6 ESMs. **c**, Density scatter plot of observation-based and simulated baseflow indices. **d**, Latitudinal profiles of the CMIP6-simulated baseflow indices. The black line and grey shading represent mean ± standard deviation. MAPE, mean absolute percentage error.

the black regression line, providing evidence for the validity of the emergent constraint relationship.

Furthermore, we constructed emergent constraint relationships of 17 major rivers using their internal small basins (Extended Data Table 2). Three of the 17 major rivers possess tracer-based baseflow index estimates: 70%, 57% and 56% for the Amazon[29], Missouri[30] and Upper Colorado[11] rivers, respectively. As shown in Fig. 2b, emergent constraints in these three major rivers yield baseflow index estimates of 71%, 57% and 67%, respectively, which are consistent with the tracer-based baseflow index estimates and higher than the original ESM estimates of 56%, 35% and 41% (see Extended Data Fig. 5 for details). We also present the constrained baseflow indices for different climate zones in Extended Data Table 3.

## Lower bound of groundwater recharge

Groundwater recharge is the process by which water moves down from the surface into an aquifer. This recharged water, apart from being consumed by evapotranspiration or withdrawn via wells, is discharged into oceans or rivers. Consequently, the groundwater discharged into rivers (baseflow) represents the numerical lower bound of groundwater recharge[31,32]. Due to the scarcity of measurements, previous global groundwater recharge estimates have relied primarily on global hydrological models (Extended Data Table 4). Here we multiply the constrained baseflow index by run-off coefficients (ratio of run-off to precipitation) to derive a lower bound for the global groundwater recharge ratio (recharge as a proportion of precipitation). We used three run-off coefficients derived from different forcing datasets, leading to a lower bound estimate of 21% ± 3% for the global recharge ratio (see Methods for the uncertainty estimate). Notably, all calculations were performed in areas without continuous permafrost, and we demonstrate that excluding permafrost does not greatly impact the lower bound estimate. Assuming baseflow index values of 0 or 1 for these permafrost areas turns the 21% into 20% or 22%, respectively.

The baseflow-derived lower bound recharge ratio estimate of 21% suggests that the global water-cycle diagram of the IPCC Sixth Assessment Report may have underestimated the recharge ratio (dividing the reported groundwater recharge flux of 13,000 $km^3\ yr^{-1}$ by land precipitation of 120,000 $km^3\ yr^{-1}$ yields a recharge ratio of 11%). Thus, our findings suggest that groundwater contributions to evapotranspiration and streamflow may be substantially greater (nearly two times higher) than suggested by the IPCC Sixth Assessment Report. Our conclusion—that real-world groundwater recharge is greater than suggested by the IPCC Sixth Assessment Report—is consistent with a recent study comparing groundwater recharge rates based on measurements versus those simulated by global hydrological models[33].

https://doi.org/10.1038/s41561-024-01483-5

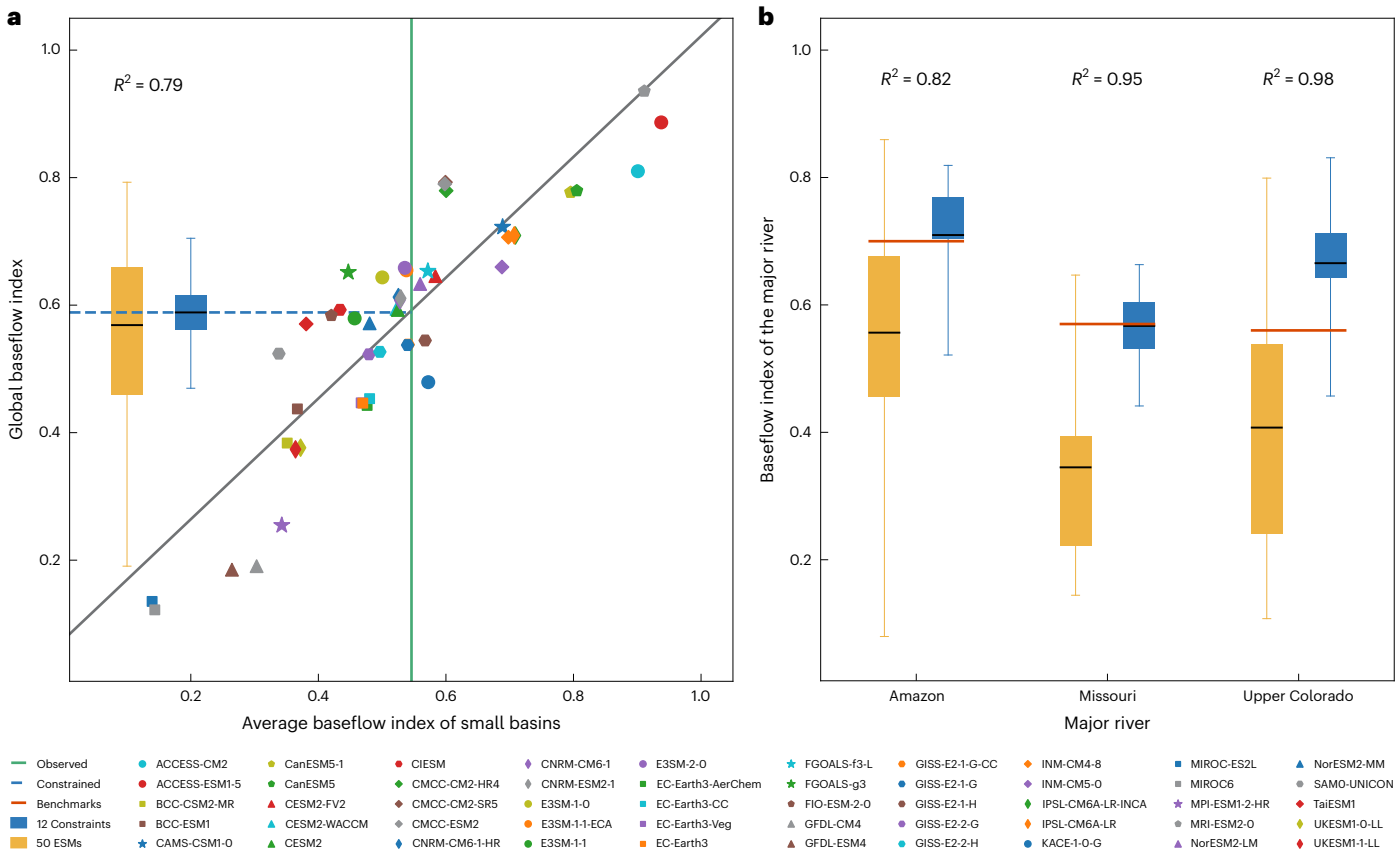


**Fig. 2 | Emergent constraints on the baseflow index. a**, On the global scale. Each scatter represents an ESM. For a specific ESM, the *x* axis represents its simulated mean baseflow index across 15,496 small basins, and the *y* axis represents the simulated global baseflow index. The black regression line depicts the relationship between the *x*- and *y*-axes variables for the 50 ESMs. The vertical green line at 55% corresponds to the observation-based mean baseflow index across the 15,496 basins, calculated as an average from 12 baseflow separation methods. The horizontal blue dotted line is obtained by substituting 55% into the regression relationship, indicating the global baseflow index estimate of 59% through emergent constraint. The blue box represents 12 constrained estimates of the global baseflow index from 12 vertical green lines (not shown), each corresponding to the mean baseflow index across basins for one baseflow separation method. The yellow box represents 50 global baseflow index estimates from ESMs. The horizontal line within each box represents the mean baseflow index estimates, and the box lengths encompass the first to third quartiles. The whiskers of boxes do not exceed 1.5 times the box lengths. Outliers beyond the whiskers are not displayed here. **b**, Comparison of constrained and tracer-based baseflow index estimates in three major rivers. The red lines denote the tracer-based baseflow index estimates from the literature review. Yellow and blue boxes represent baseflow index estimates from 50 ESMs and 12 constraints, respectively, and share the same box length, centre and whisker settings as plot **a**. Detailed emergent constraints for the three rivers are presented in Extended Data Fig. 5.

## Potential causes of model discrepancies

ESMs simulated five baseflow generation processes: (1) infiltration, (2) lower boundary conditions that determine how the aquifer stores groundwater (3) groundwater dynamics for baseflow calculations, (4) soil water transmission and (5) root water uptake. The primary differences between ESMs lie in the first three processes because most ESMs utilize Richards' equation for (4) and disregard the soil–root hydraulic gradient for (5)[15]. To assess the impact of different representations of these processes on baseflow, we investigated three ESMs: CESM2, MIROC6 and ACCESS-ESM1-5. These ESMs correspond to the land surface models of CLM5.0, MATSIRO6 and CABLE, with global baseflow indices of 59% (matching the constrained baseflow index), 12% (substantial underestimation) and 89% (large overestimation), respectively.

Regarding (1) infiltration, CABLE requires the upper three soil layers (0.234 m) to be 95% saturated for surface run-off to occur[34], while both CLM5.0 and MATSIRO6 use empirical functions to relate the percentage saturated area to water-table depth. This disparity in infiltration may account for the higher baseflow index of CABLE. For the (2) lower boundary conditions, CLM4.5 employs a free drainage boundary that overlooks upward capillary flow, leading to increased baseflow in shallow bedrock areas. CLM5.0 addresses this limitation by introducing variable soil thickness, enabling explicit modelling of saturated and unsaturated zones[35,36]. This improvement is probably responsible for the lower baseflow index estimates based on CLM5.0 compared with CLM4.5 (for example, 59% for CESM2 versus 79% for CMCC-ESM2). In terms of the (3) groundwater dynamics process, MATSIRO6 uses a simplified TOPMODEL to link baseflow with hydraulic conductivity[37]. MATSIRO6 nearly doubles the coefficient that characterizes the decay of hydraulic conductivity with soil depth. This modification, as described in equation 9.22 of the MATSIRO6 document[38], could potentially explain why the baseflow index of MIROC6 (12%) is lower compared with that of MIROC5 (34%).

Diverse process representations lead to different contributions of environmental drivers to spatial variations in baseflow, as uncovered by explainable machine learning (Methods). We used 18 environmental drivers similar to previous studies[12,37]. As shown in Fig. 3a, soil (aggregation of six soil drivers in Extended Data Table 5) emerges as the largest contributor, interpreting 31% of observation-based spatial variations. Conversely, most ESMs identify water (aggregation of precipitation and snowfall) as the primary contributor, attributing at least 30% to the simulated spatial variations. Figure 3b provides further insights into

https://doi.org/10.1038/s41561-024-01483-5

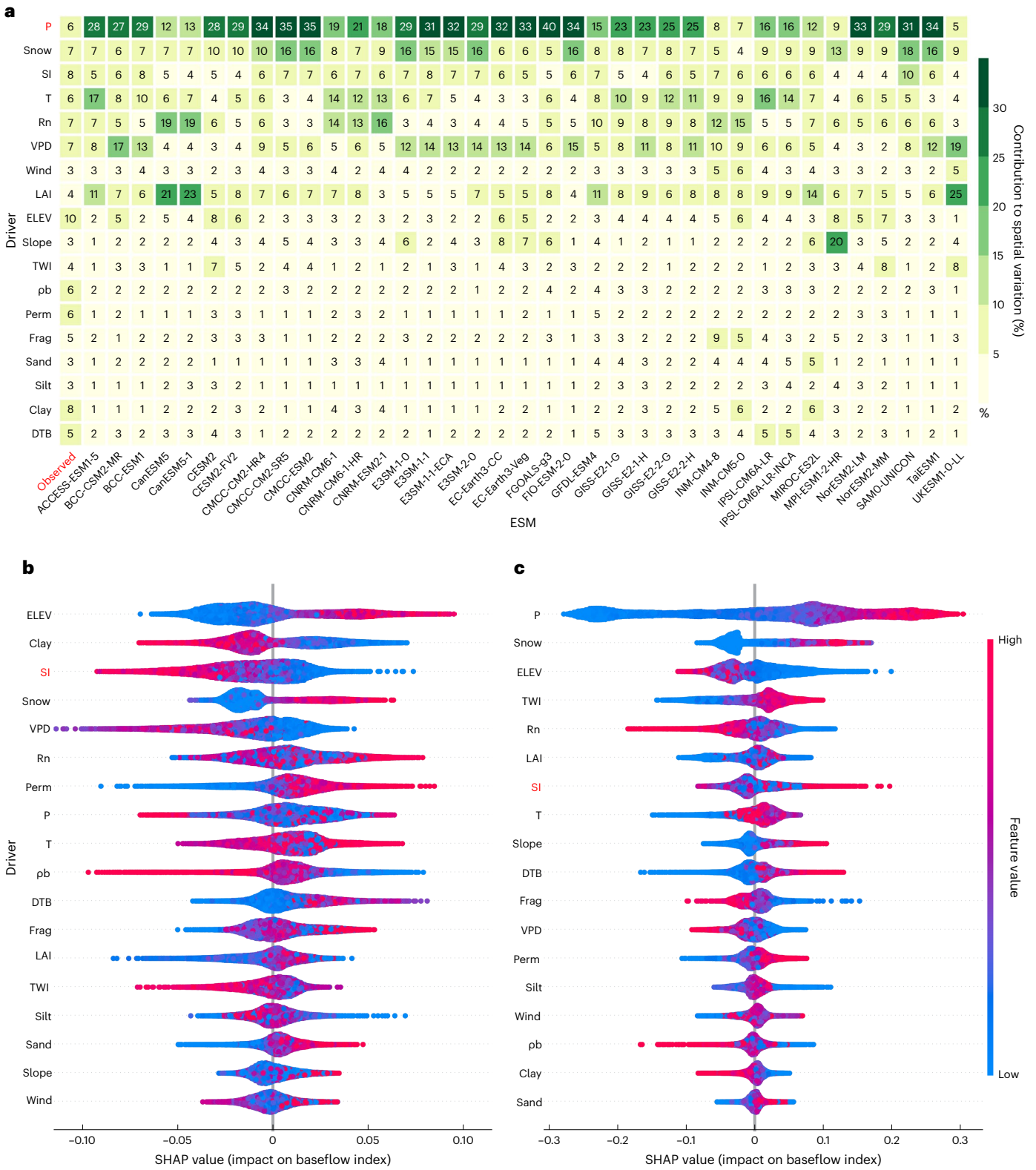


**Fig. 3 | Contribution of environmental drivers to baseflow index spatial variations. a**, Cumulative percentage contributions of 18 environmental drivers in a Mollweide equal-area projection for all 3,080 km$^2$ grids globally, excluding areas with continuous permafrost. The *y*-axis labels are abbreviations of the 18 drivers, with detailed descriptions in Extended Data Table 5. The first column, highlighted in red, shows the driver contributions to observational-based spatial variations. The other columns represent 37 ESMs, with the remaining 13 ESMs excluded due to missing drivers. Precipitation is highlighted in red to indicate the large difference between its contributions to observational-based and simulated spatial variations. **b**,**c**, Shapley Additive Explanations (SHAP; Methods) plots for the observation-based (**b**) and CESM2 (**c**) baseflow indices. The 18 drivers are ranked on the basis of their cumulative global contributions. Each dot represents a 3,080 km$^2$ grid. The dot colour indicates the value of the corresponding driver, and its *x*-axis value represents the SHAP value that quantifies the driver's impact on the baseflow index for that grid. The precipitation seasonality index (SI) is marked in red to highlight the opposite patterns revealed by the observation-based SHAP and the CESM2 SHAP. The observation-based SHAP shows that seasonality contributes negatively to the baseflow index, as evidenced by red dots located to the left of blue dots, while CESM2 SHAP does the opposite.

https://doi.org/10.1038/s41561-024-01483-5

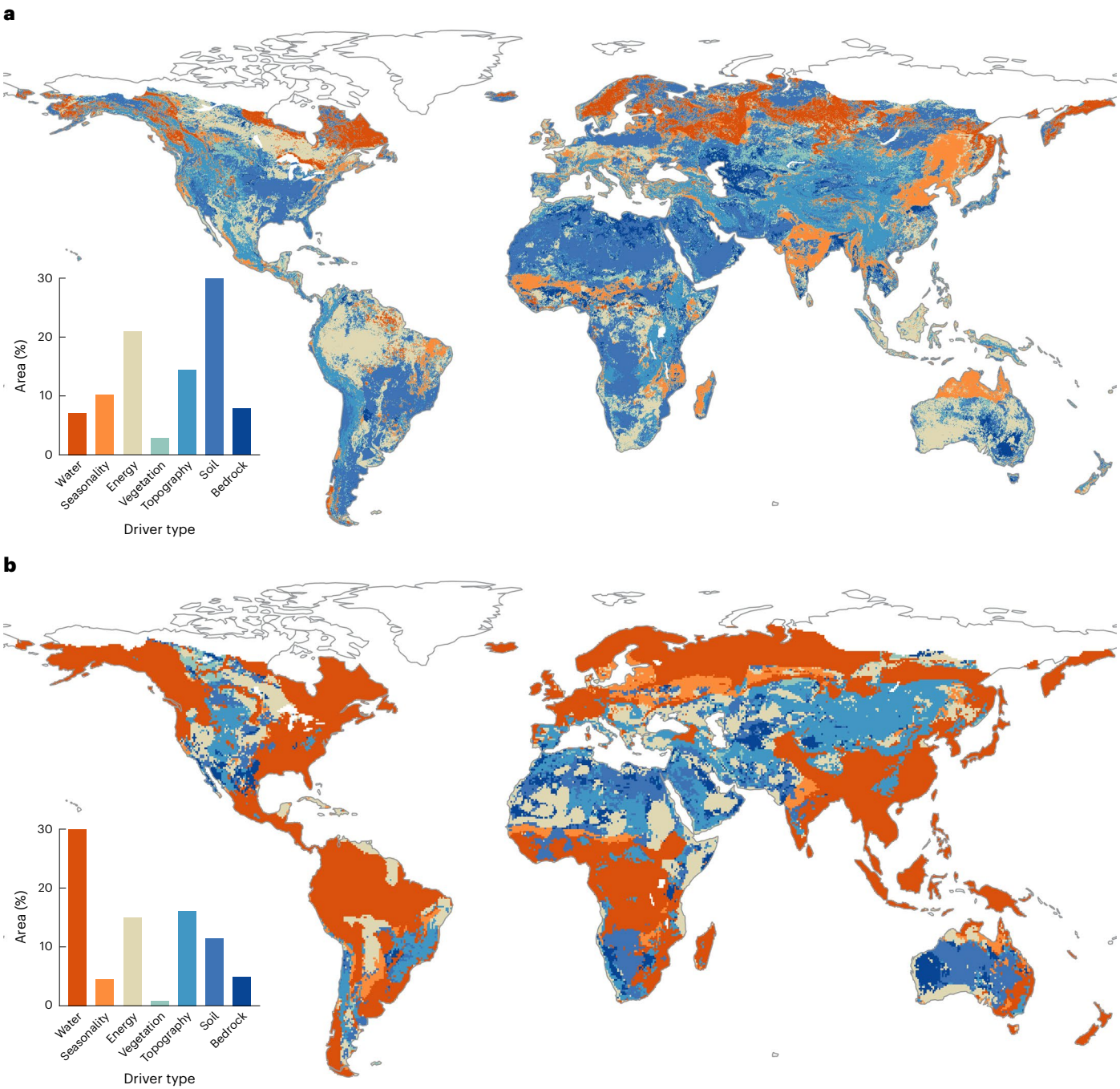


**Fig. 4 | Global spatial distribution of baseflow index dominant factors.** **a**, For the observation-based baseflow index. **b**, For the CESM2 baseflow index. The 18 environmental drivers are classified into seven types, as listed in Extended Data Table 5. The legend indicating the area percentages of the seven types has been truncated below 30 to enhance readability. Soil dominated 37% and 11% of the area for the observation-based and CESM2 baseflow index, respectively, whereas seasonality dominated 10% and 4%, respectively. Water dominated only 7% of the area for the observation-based baseflow index, located primarily in snowy areas at high latitudes, compared with 46% for the CESM2 baseflow index. The observation-based dominant factors seem to be more reasonable. Soil and seasonality directly affect infiltration and thus may be more influential on the baseflow index than is precipitation magnitude.

the positive or negative impact of environmental drivers on baseflow indices. The observation-based impact plot reveals that precipitation seasonality contributes negatively to the baseflow index, consistent with the fact that more concentrated precipitation in certain months lowers the baseflow index, while CESM2 presents the opposite result to the fact. Figure 4 spatially illustrates the CESM2's overestimation of precipitation impacts. Soil dominates 37% of the area for the observation-based baseflow index, while water dominates 46% of the area for CESM2. The observation-based dominant factors seem to be more reasonable. For example, precipitation magnitude may have a smaller impact on the baseflow index than soil, which directly affects infiltration. Greater precipitation magnitude may raise or lower the baseflow index, depending on the seasonal distribution of precipitation.

## Implications for groundwater simulation

Our analysis shows that groundwater sustains 59% ± 7% of global river flows. This proportion ranges widely for ESM simulations, from 12% to 94%, which may be attributed to diverse representations of infiltration,

aquifer structure and groundwater dynamics. For example, few if any simulations adequately capture the role of macropores as a key if not fundamental factor determining actual infiltration rates[39]. The key role of macropores has been overlooked for decades[40], and there remains substantial room for improvement in the characterization of their abundance (via field measurements) and the simulation of their hydrological functions in ESMs. Below the soil profile, the oversimplified representation of hydrogeologic conditions (for example, hydraulic conductivity and its heterogeneity) in many models may also play a role in driving discrepancies between simulated hydrology and real-world conditions. Further research—such as this study's approach—bringing together real-world measurements and model simulations may help to improve hydrological simulations of ESMs and thus improve the credibility of their projections.

Future enhancements to model representations of groundwater–river connections could involve implementation of fast infiltration through macropores[41], incorporation of interactions between groundwater and vegetation[42,43], improved characterization of spatial heterogeneity such as aquifer transmissivity[44], and introduction of Darcy's law into groundwater dynamics[37]. Such enhancements may make model outputs more relevant to real-world water management and forecasting.

## Online content

Any methods, additional references, Nature Portfolio reporting summaries, source data, extended data, supplementary information, acknowledgements, peer review information; details of author contributions and competing interests; and statements of data and code availability are available at https://doi.org/10.1038/s41561-024-01483-5.

## References


1. Alley, W. M., Healy, R. W., LaBaugh, J. W. & Reilly, T. E. Flow and storage in groundwater systems. *Science* **296**, 1985–1990 (2002).
2. Winter, T. C., Harvey, J. W., Franke, O. L. & Alley, W. M. *Ground Water and Surface Water: A Single Resource* Circular 1139 (USGS, 1998); https://doi.org/10.3133/cir1139
3. Dunne, T. & Leopold, L. B. *Water in Environmental Planning* (Macmillan, 1978).
4. Beven, K. The era of infiltration. *Hydrol. Earth Syst. Sci.* **25**, 851–866 (2021).
5. Horton, R. E. Remarks on hydrologic terminology. *EOS Trans. Am. Geophys. Union* **23**, 479–482 (1942).
6. Sánchez-Murillo, R. *Natural and Human Influences on Baseflow Regimes: A Physically-Based and Geochemical Analysis*. PhD dissertation, Univ. Idaho (2014).
7. Jasechko, S., Seybold, H., Perrone, D., Fan, Y. & Kirchner, J. W. Widespread potential loss of streamflow into underlying aquifers across the USA. *Nature* **591**, 391–395 (2021).
8. Jasechko, S. et al. Global aquifers dominated by fossil groundwaters but wells vulnerable to modern contamination. *Nat. Geosci.* **10**, 425–429 (2017).
9. Jasechko, S., Kirchner, J. W., Welker, J. M. & McDonnell, J. J. Substantial proportion of global streamflow less than three months old. *Nat. Geosci.* **9**, 126–129 (2016).
10. Berghuijs, W. R. & Slater, L. J. Groundwater shapes North American river floods. *Environ. Res. Lett.* **18**, 034043 (2023).
11. Miller, M. P., Buto, S. G., Susong, D. D. & Rumsey, C. A. The importance of base flow in sustaining surface water flow in the Upper Colorado River basin. *Water Resour. Res.* **52**, 3547–3562 (2016).
12. Beck, H. E. et al. Global patterns in base flow index and recession based on streamflow observations from 3394 catchments. *Water Resour. Res.* **49**, 7843–7863 (2013).
13. Rodell, M. et al. The global land data assimilation system. *Bull. Am. Meteorol. Soc.* **85**, 381–394 (2004).
14. IPCC *Climate Change 2021: The Physical Science Basis* (eds Masson-Delmotte, V. et al.) (Cambridhe Univ. Press, 2021).
15. Clark, M. P. et al. Improving the representation of hydrologic processes in Earth system models. *Water Resour. Res.* **51**, 5929–5956 (2015).
16. Genereux, D. Quantifying uncertainty in tracer-based hydrograph separations. *Water Resour. Res.* **34**, 915–919 (1998).
17. Lott, D. A. & Stewart, M. T. Base flow separation: a comparison of analytical and mass balance methods. *J. Hydrol.* **535**, 525–533 (2016).
18. Lyne, V. & Hollick, M. Stochastic time-variable rainfall-runoff modelling. In *Proc. Institute of Engineers Australia National Conference* 89–93 (Institute of Engineers Australia, 1979).
19. Nathan, R. J. & McMahon, T. A. Evaluation of automated techniques for base flow and recession analyses. *Water Resour. Res.* **26**, 1465–1473 (1990).
20. Gonzales, A. L., Nonner, J., Heijkers, J. & Uhlenbrook, S. Comparison of different base flow separation methods in a lowland catchment. *Hydrol. Earth Syst. Sci.* **13**, 2055–2068 (2009).
21. Rutledge, A. T. *Computer Programs for Describing the Recession of Ground-Water Discharge and for Estimating Mean Ground-Water Recharge and Discharge from Streamflow Records-Update* (USGS, 1998); https://doi.org/10.3133/wri984148
22. Santhi, C., Allen, P. M., Muttiah, R. S., Arnold, J. G. & Tuppad, P. Regional estimation of base flow for the conterminous United States by hydrologic landscape regions. *J. Hydrol.* **351**, 139–153 (2008).
23. Wolock, D. M. *Base-Flow Index Grid for the Conterminous United States* (USGS, 2003); http://pubs.er.usgs.gov/publication/ofr03263
24. Zhang, J. et al. Large-scale baseflow index prediction using hydrological modelling, linear and multilevel regression approaches. *J. Hydrol.* **585**, 124780 (2020).
25. Cox, P. M. et al. Sensitivity of tropical carbon to climate change constrained by carbon dioxide variability. *Nature* **494**, 341–344 (2013).
26. Hall, A., Cox, P., Huntingford, C. & Klein, S. Progressing emergent constraints on future climate change. *Nat. Clim. Change* **9**, 269–278 (2019).
27. Shiogama, H., Watanabe, M., Kim, H. & Hirota, N. Emergent constraints on future precipitation changes. *Nature* **602**, 612–616 (2022).
28. Lian, X. et al. Partitioning global land evapotranspiration using CMIP5 models constrained by observations. *Nat. Clim. Change* **8**, 640–646 (2018).
29. Mortatti, J., Moraes, J. M., Rodrigues, J., Victoria, R. L. & Martinelli, L. A. Hydrograph separation of the Amazon River using $^{18}O$ as an isotopic tracer. *Sci. Agric.* **54**, 167–173 (1997).
30. Yang, W., Xiao, C. & Liang, X. Technical note: analytical sensitivity analysis and uncertainty estimation of baseflow index calculated by a two-component hydrograph separation method with conductivity as a tracer. *Hydrol. Earth Syst. Sci.* **23**, 1103–1112 (2019).
31. Arnold, J. G. & Allen, P. M. Automated methods for estimating baseflow and ground water recharge from streamflow records. *J. Am. Water Resour. Assoc.* **35**, 411–424 (1999).
32. Gleeson, T. et al. GMD perspective: the quest to improve the evaluation of groundwater representation in continental- to global-scale models. *Geosci. Model Dev.* **14**, 7545–7571 (2021).
33. Berghuijs, W. R., Luijendijk, E., Moeck, C., van der Velde, Y. & Allen, S. T. Global recharge data set indicates strengthened groundwater connection to surface fluxes. *Geophys. Res. Lett.* **49**, e2022GL099010 (2022).

34. Decker, M. Development and evaluation of a new soil moisture and runoff parameterization for the CABLE LSM including subgrid-scale processes. *J. Adv. Model. Earth Syst.* **7**, 1788–1809 (2015).
35. Brunke, M. A. et al. Implementing and evaluating variable soil thickness in the Community Land Model, Version 4.5 (CLM4.5). *J. Clim.* **29**, 3441–3461 (2016).
36. Lawrence, D. M. et al. The Community Land Model Version 5: description of new features, benchmarking, and impact of forcing uncertainty. *J. Adv. Model. Earth Syst.* **11**, 4245–4287 (2019).
37. Tashie, A., Pavelsky, T. & Kumar, M. A calibration-free groundwater module for improving predictions of low flows. *Water Resour. Res.* **58**, e2021WR030800 (2022).
38. Guo, Q. et al. Description of MATSIRO6. *UTokyo Repository* https://doi.org/10.15083/0002000181 (2021).
39. Beven, K. & Germann, P. Macropores and water flow in soils. *Water Resour. Res.* **18**, 1311–1325 (1982).
40. Beven, K. & Germann, P. Macropores and water flow in soils revisited. *Water Resour. Res.* **49**, 3071–3092 (2013).
41. Gharari, S. et al. Improving the representation of subsurface water movement in land models. *J. Hydrometeorol.* **20**, 2401–2418 (2019).
42. Fan, Y. et al. Hillslope hydrology in global change research and Earth system modeling. *Water Resour. Res.* **55**, 1737–1772 (2019).
43. Fan, Y., Miguez-Macho, G., Jobbágy, E. G., Jackson, R. B. & Otero-Casal, C. Hydrologic regulation of plant rooting depth. *Proc. Natl Acad. Sci. USA* **114**, 10572–10577 (2017).
44. Hartmann, A., Gleeson, T., Wada, Y. & Wagener, T. Enhanced groundwater recharge rates and altered recharge sensitivity to climate variability through subsurface heterogeneity. *Proc. Natl Acad. Sci. USA* **114**, 2842–2847 (2017).

# Methods

## Observational data

We collected daily streamflow records for 48,651 basins from 9 national agencies and 3 research databases: (1) 4,467 basins from the Australian Bureau of Meteorology; (2) 3,520 basins from the Brazilian Agência Nacional de Águas; (3) 5,783 basins from the National Water Data Archive of Canada; (4) 515 basins from the Chilean Center for Climate and Resilience Research; (5) 314 basins from the Chinese Ministry of Water Resources; (6) 368 basins from the Indian Water Resources Information System; (7) 1,363 basins from Spanish Centro de Estudios Hidrográficos; (8) 1,565 basins from the UK National River Flow Archive; (9) 23,489 basins from the US National Water Information System; (10) 135 basins in the Network for the Arctic Region database; (11) 2,460 basins in the European Water Archive; (12) 4,672 basins from the Global Runoff Data Centre. We eliminated duplicates in the last three research databases using the procedures outlined in ref. 45. The 48,651 basin boundaries were delineated using an automatic outlet relocation method[46]. We applied the following criteria to select basins for analysis: (1) the basin area is smaller than 2,500 km$^2$ to minimize the impact of river channel routing; (2) at least 5 years of consecutive daily streamflow observations are available from 1950 to 2022; (3) the reservoir capacity within the basin is less than 10% of the annual mean streamflow, as determined by the Global Reservoir and Dam database v.1.3[47]; (4) the urban area is less than 5% of the total basin area according to the Moderate Resolution Imaging Spectroradiometer Land Cover Type v.6.1[48]; (5) it satisfies $R < P$ and $R + \mathrm{PET} > P$ to ensure the accuracy of basin boundaries, where $R$, $P$ and PET are run-off depth, precipitation and potential evapotranspiration, respectively. These criteria screened 15,496 small basins with limited anthropogenic interventions for baseflow separation.

We used 5 yr streamflow records as the basin selection threshold to trade off the basins' spatial coverage and the streamflow's temporal length. A 10 yr threshold, while providing a longer temporal perspective, would unfortunately lead to the exclusion of numerous basins in Africa, Central Asia and East Asia, as indicated by the red dots in Extended Data Fig. 3b. The density scatter plot in Extended Data Fig. 3f validates that the 5 yr baseflow indices can effectively capture the global spatial variations of baseflow indices. Despite efforts to gather streamflow data, the 15,496 basins still have limitations in providing a truly global view of baseflow estimates. One such limitation is the lack of streamflow observations in many irrigated areas around the globe (for example, areas within China and the Middle East). This gap in data coverage may substantially impact the accuracy of global baseflow index estimates, given the pivotal role of irrigation in water-cycle dynamics[49]. Future research may bridge the gap by incorporating irrigation-related data into the global baseflow assessment.

Environmental drivers, including eight multi-year averages and ten static properties, were used to investigate their contributions to baseflow index spatial variations. Extended Data Table 5 provides detailed descriptions of these 18 environmental drivers, similar to those used by refs. 12,50. The eight multi-year averages were computed using the European Centre for Medium-Range Weather Forecasts Reanalysis Version 5 Land (ERA5-Land) monthly dataset, which covers the period from 1950 to the present at a spatial resolution of 0.1°. To align with the end year of CMIP6 historical outputs, we restricted the ERA5-Land dataset to the period between 1950 and 2014. For each basin, we calculated area-weighted averages for these gridded environmental drivers, serving as the training data for modelling baseflow index spatial variations.

Uncertainty in the lower bound of the global groundwater recharge ratio was calculated using a run-off ensemble called G-RUN ENSEMBLE, which has 21 gridded run-off simulations driven by different forcing datasets[51]. Only three forcing datasets from different institutes cover the period 1950 to 2014, including Climatic Research Unit gridded Time Series Version 4.04[52], Global Soil Wetness Project Phase 3[53] and Princeton Global Forcing Version 3[54]. On the basis of the precipitation and driven G-RUN run-off from these three datasets, we obtained run-off coefficients of 35.0%, 35.4% and 34.6%, respectively, for areas without continuous permafrost (excluded in the same way as refs. 55,56). Hence, 36 combinations of 12 constrained baseflow indices and 3 run-off coefficients yield a lower bound of 21% ± 3% (mean ± standard deviation) for the global groundwater recharge ratio. The multimodel median of G-RUN ENSEMBLE was also used as weights to calculate a global baseflow index of 71% for the map of ref. 12.

## CMIP6 model simulations

We used the variables 'mrro' and 'mrros' to calculate baseflow indices for 50 CMIP6 ESMs, where mrro represents total run-off and mrros represents surface run-off. The 50 ESMs and their coupled land surface models are listed in Extended Data Table 1. It is important to note that the difference between mrro and mrros corresponds to baseflow, although this difference could also include subsurface stormflow. On careful examination of the documents and source codes of the ESMs, we have discovered that the majority of ESMs do not simulate subsurface stormflow, as demonstrated by equation 9.14 in MIROC6 and figure 2.2 in MPI-ESM1-2-HR[38,57]. However, the term 'surface run-off' historically carries an ambiguous definition. It is perceptually understood as the run-off generated over the land surface. Yet hydrologists initially defined it as the run-off that contributes to the hydrograph, encompassing subsurface stormflow. For example, ref. 5 pointed out that water contributing to the hydrograph may flow into channels through subsurface pathways such as Sun cracks. This type of water, referred to as subsurface stormflow, follows the same laws as visible surface run-off. Hence, it is more appropriate to treat subsurface stormflow as 'concealed surface run-off.' Given this ambiguous definition of surface run-off, ref. 4 explicitly suggested the terms 'overland flow' and 'subsurface stormflow' instead of surface run-off. In summary, considering the implementation and definition of subsurface stormflow in ESMs, the difference between mrro and mrros matches well with baseflow.

To compare the contributions of environmental drivers with the observation-based and simulated baseflow index, we also gathered the eight multi-year averages listed in Extended Data Table 5 from CMIP6 as an alternative to ERA5-Land. Alongside these distinct multi-year averages, the observation-based and simulated baseflow indices were trained on the same ten static properties using machine learning. All CMIP6 variables were first regridded to 0.5° resolution using linear interpolation through the ESM Evaluation Tool[58] and then aggregated as multi-year averages from 1950 to 2014.

## Baseflow separation

To make the baseflow separation results as representative as possible of the actual baseflow index, we used 12 typical baseflow separation methods that can return reproducible results. These 12 methods comprise 4 graphical methods and 8 digital filter methods. The four graphic methods are the smooth minima method developed by the UK Institute of Hydrology[59] and three methods (fixed interval, sliding interval and local minimum) developed by the US Geological Survey[60]. They share the same step of separating baseflow from hydrograph by connecting specific low-flow points, differing only in the selection of low-flow points. The eight digital filter methods use signal analysis to separate baseflow from daily streamflow, assuming that baseflow is the low-frequency component of streamflow[18,61–67]. They typically involve one or two parameters, such as the recession constant. We employed the Brutsaert approach to automatically estimate the recession constant[68]. As for the second parameter, we utilized a multi-objective optimization approach proposed by ref. 69 to calibrate them. This optimization approach, when applied to a two-parameter digital filter developed by ref. 67, produced baseflow results that have a fair agreement with tracer-based baseflow. The multi-objective optimization has the following loss function:

$$\text{loss} = 1 - \left(1 - \frac{1 - \text{NSE}_{\text{recession}}}{1 - \text{NSE}_{\text{other}}}\right) \times (1 - f_{\text{exceed}}) \quad (1)$$

where $\text{NSE}_{\text{recession}}$ is the Nash–Sutcliffe efficiency (NSE) between baseflow and streamflow during recession periods. We used an automatic algorithm to identify a set of recession periods[70]. $\text{NSE}_{\text{other}}$ refers to the NSE calculated for the non-recession periods when stormflow exists; $f_{\text{exceed}}$ denotes the fraction of days in which estimated baseflow exceeds streamflow. The loss function aims to achieve three objectives: (1) fit the estimated baseflow to streamflow during recession periods; (2) ensure a noticeable separation between the estimated baseflow and streamflow during non-recession periods; (3) attempt to prevent the estimated baseflow from surpassing streamflow. All the 12 baseflow separation methods and automatic parameter estimation approaches adhere to their original literature. We have implemented these methods as a Python package (https://pypi.org/project/baseflow).

### Emergent constraint

We used an emergent constraint approach to relate the baseflow indices of small basins to the global baseflow index. The emergent constraint approach not only yields a new estimate of the global baseflow index but also reduces uncertainty within an ensemble of ESMs[25–28,71]. The core concept of this approach is that, although a large ensemble of ESMs will inevitably produce a broad range of estimates for a particular variable $Y$, a discernible relationship between $Y$ and another variable $X$ may emerge in ESM simulations. Usually, $Y$ is an unobservable variable, for example, the global baseflow index in this study; $X$ is an observable or easily computed variable, for example, the mean baseflow index across the 15,496 basins. Once we identify the relationship between $Y$ and $X$ using exclusively simulations from the large ensemble of ESMs, we can then plug in observations of variable $X$ to narrow the estimate of variable $Y$. Here we separated baseflow from daily streamflow observations of the 15,496 basins, treating the mean baseflow index across these basins as the observation of variable $X$. We employed 12 baseflow separation methods, each corresponding to an observation of variable $X$. These observations were subsequently incorporated into the relationship between $Y$ and $X$, resulting in a refined estimate of the global baseflow index with reduced uncertainty. We acknowledge that the uncertainty in our constrained global baseflow index may be underreported if missing or oversimplified processes shared among ESMs lead the emergent constraint relationship to deviate from reality[72].

### Explainable machine learning

We used a machine-learning approach called Extreme Gradient Boosting (XGBoost) to establish a relationship between baseflow indices and the 18 environmental drivers[73]. XGBoost offers two distinct advantages over the traditional Random Forest approach. (1) Random Forest and XGBoost are both powerful ensemble methods but with different strategies (bagging and boosting). Random Forest creates parallel decision trees and uses subsets of samples to generate several predictions, which are then combined using methods such as averaging or voting. XGBoost constructs sequential trees and fits the residuals of previous trees, focusing on poorly understood fields. (2) XGBoost employs the Taylor series to approximate the loss function, providing the flexibility to use a variety of loss functions. This flexibility empowers us to tune multiple loss functions. We carefully tuned XGBoost hyperparameters, including the selection of the square logarithmic loss function, 2,000 trees and a learning rate of 0.055. We implemented tenfold cross-validation to assess model performance, which consisted of three processes: (a) randomly dividing the 15,496 basins into ten groups of equal size; (b) selecting nine groups as training data to fit the XGBoost model, while the remaining group served as unseen data for model evaluation (this process iterated until each group had been selected as unseen data once); (c) computing the average of model performance metrics across the ten evaluation iterations. The XGBoost model achieved an $R^2$ value of 0.72 ($P < 0.001$), a mean absolute error of 0.04 and a Kling–Gupta efficiency[74] of 0.78, demonstrating its effectiveness in simulating baseflow indices.

In addition, we used Shapley Additive Explanations (SHAP) to quantify the contributions of the 18 environmental drivers to spatial variations in baseflow indices[75]. Compared with other machine-learning interpretation methods, SHAP offers the advantage of identifying contributions at a micro level (for example, individual grids). For a specific 3,080 km$^2$ grid in the Mollweide equal-area projection, its simulated baseflow index is determined by adding a baseline value (the average simulated baseflow index for all global grids) to the SHAP values of 18 environmental drivers, as shown in the following equation:

$$\text{BFI}_i = \overline{\text{BFI}} + \text{SHAP}_T + \text{SHAP}_{\text{ELEV}} + \text{SHAP}_{\text{SI}} + \cdots \quad (2)$$

where $\text{BFI}_i$ is the baseflow index for the specific grid, $\overline{\text{BFI}}$ is the baseline value, $\text{SHAP}_T$, $\text{SHAP}_{\text{ELEV}}$ and $\text{SHAP}_{\text{SI}}$ correspond to the SHAP values of temperature, elevation and precipitation seasonality index, respectively. Other drivers have similar notations and are omitted here. Although the SHAP values are obtained through a game-theoretic approach involving all grids, we can regard them as the impact of environmental drivers on the baseflow index for a specific grid. To determine the overall contribution of temperature, we sum the absolute values of $\text{SHAP}_T$ for each grid. Then we divide this sum by the total absolute SHAP value to convert it to a percentage. The same process is applied to the other drivers, leading to the percentage contributions in Fig. 3. By leveraging the additivity property of SHAP, we aggregate the SHAP values to obtain the importance for an entire group of drivers. This enables us to plot the dominant factors influencing the baseflow index in Fig. 4.

## Data availability

Our research benefits from the following data sources: (1) daily streamflow records for 48,651 basins from 9 national agencies and 3 research databases: Australian Bureau of Meteorology (http://www.bom.gov.au/waterdata/), Brazilian Agência Nacional de Águas (https://zenodo.org/record/3964745)[76], National Water Data Archive of Canada (https://wateroffice.ec.gc.ca/), Chilean Center for Climate and Resilience Research (https://doi.org/10.1594/PANGAEA.894885), Chinese Ministry of Water Resources (http://www.cjh.com.cn/), Indian Water Resources Information System (https://indiawris.gov.in/wris/#/RiverMonitoring), Spanish Centro de Estudios Hidrográficos (https://ceh.cedex.es/anuarioaforos/demarcaciones.asp), UK National River Flow Archive (https://nrfaapps.ceh.ac.uk/nrfa/nrfa-api.html), US National Water Information System (https://waterdata.usgs.gov/nwis), Network for the Arctic Region (ArcticNET) database (https://www.r-arcticnet.sr.unh.edu/), the European Water Archive (https://ne-friend.bafg.de/servlet/is/7413/), the Global Runoff Data Centre (https://www.bafg.de/GRDC); (2) the ERA5-Land monthly dataset (https://cds.climate.copernicus.eu/cdsapp#!/dataset/reanalysis-era5-land-monthly-means); (3) the CMIP6 historical outputs for the 50 ESMs (https://esgf-node.llnl.gov/search/cmip6/); (4) 3 run-off simulations from G-RUN ENSEMBLE (https://doi.org/10.6084/m9.figshare.12794075)[77], driven by precipitation from Climatic Research Unit gridded Time Series Version 4.04 (https://crudata.uea.ac.uk/cru/data/hrg/cru_ts_4.04/), Global Soil Wetness Project Phase 3 (https://doi.org/10.20783/DIAS.501) and Princeton Global Forcing Version 3 (https://prep-next.github.io/data/GDFC/products.html); (5) the global baseflow index map using artificial neural networks to extend from 3,394 basins to global grids (https://www.gloh2o.org/gscd/); (6) the Noah Land Surface Model outputs from the Global Land Data Assimilation System Version 2.0 (https://ldas.gsfc.nasa.gov/gldas); (7) static properties listed in Extended Data Table 5: Multi-Error-Removed Improved-Terrain digital elevation model (https://hydro.iis.u-tokyo.ac.jp/~yamadai/MERIT_DEM/), topographic wetness index from

Geomorpho90m (https://doi.org/10.1594/PANGAEA.899135), soil properties form SoilGrids 2.0 (https://soilgrids.org/), logarithmic permeability from global hydrogeology (https://borealisdata.ca/dataset.xhtml?persistentId=doi:10.5683/SP2/TTJNIU) and bedrock depth map (https://files.isric.org/soilgrids/former/2017-03-10/data/BDTICM_M_250m_ll.tif).

## Code availability

The 12 baseflow separation methods are implemented as a Python package at https://github.com/xiejx5/baseflow. The automatic basin boundary delineation algorithm was shared at https://github.com/xiejx5/watershed_delineation. We express our gratitude to the following open-source projects for their valuable contributions: (1) the ESM Evaluation Tool (ESMValTool) used for CMIP6 data downloading and processing (https://github.com/ESMValGroup/ESMValTool); (2) the XGBoost Python package (https://github.com/dmlc/xgboost); (3) the SHAP Python package (https://github.com/slundberg/shap).

## References


45. Gudmundsson, L. & Seneviratne, S. I. Observation-based gridded runoff estimates for Europe (E-RUN version 1.1). *Earth Syst. Sci. Data* **8**, 279–295 (2016).
46. Xie, J., Liu, X., Bai, P. & Liu, C. Rapid watershed delineation using an automatic outlet relocation algorithm. *Water Resour. Res.* **58**, e2021WR031129 (2022).
47. Lehner, B. et al. High-resolution mapping of the world's reservoirs and dams for sustainable river-flow management. *Front. Ecol. Environ.* **9**, 494–502 (2011).
48. Friedl, M. A. et al. Global land cover mapping from MODIS: algorithms and early results. *Remote Sens. Environ.* **83**, 287–302 (2002).
49. Scanlon, B. R. et al. Global water resources and the role of groundwater in a resilient water future. *Nat. Rev. Earth Environ.* **4**, 87–101 (2023).
50. Tashie, A., Pavelsky, T. & Emanuel, R. E. Spatial and temporal patterns in baseflow recession in the Continental United States. *Water Resour. Res.* **56**, e2019WR026425 (2020).
51. Ghiggi, G., Humphrey, V., Seneviratne, S. I. & Gudmundsson, L. G-RUN ENSEMBLE: a multi-forcing observation-based global runoff reanalysis. *Water Resour. Res.* **57**, e2020WR028787 (2021).
52. Harris, I., Osborn, T. J., Jones, P. & Lister, D. Version 4 of the CRU TS monthly high-resolution gridded multivariate climate dataset. *Sci. Data* **7**, 109 (2020).
53. Kim, H. *Global Soil Wetness Project Phase 3 Atmospheric Boundary Conditions (Experiment 1)* (DIAS, 2017); https://doi.org/10.20783/DIAS.501
54. He, X., Pan, M., Wei, Z., Wood, E. F. & Sheffield, J. A global drought and flood catalogue from 1950 to 2016. *Bull. Am. Meteorol. Soc.* **101**, E508–E535 (2020).
55. Gleeson, T., Moosdorf, N., Hartmann, J. & van Beek, L. P. H. A glimpse beneath earth's surface: GLobal HYdrogeology MaPS (GLHYMPS) of permeability and porosity. *Geophys. Res. Lett.* **41**, 3891–3898 (2014).
56. Gleeson, T., Befus, K. M., Jasechko, S., Luijendijk, E. & Cardenas, M. B. The global volume and distribution of modern groundwater. *Nat. Geosci.* **9**, 161–167 (2016).
57. Reick, C. H. et al. JSBACH 3—the land component of the MPI Earth System Model: documentation of version 3.2. *MPG PuRe* https://doi.org/10.17617/2.3279802 (2021)
58. Righi, M. et al. Earth System Model Evaluation Tool (ESMValTool) v2.0—technical overview. *Geosci. Model Dev.* **13**, 1179–1199 (2020).
59. *Low Flow Studies Report No. 1 Research Report* (Institute of Hydrology, 1980); http://nora.nerc.ac.uk/id/eprint/9093/
60. Sloto, R. A. & Crouse, M. Y. *HYSEP: A Computer Program for Streamflow Hydrograph Separation and Analysis* (USGS, 1996); https://doi.org/10.3133/wri964040
61. Boughton, W. The Australian water balance model. *Environ. Model. Softw.* **19**, 943–956 (2004).
62. Chapman, T. G. Comment on 'Evaluation of automated techniques for base flow and recession analyses' by R. J. Nathan and T. A. McMahon. *Water Resour. Res.* **27**, 1783–1784 (1991).
63. Chapman, T. G. & Maxwell, A. I. Baseflow separation-comparison of numerical methods with tracer experiments. In *Proc. Hydrology and Water Resources Symposium 1996: Water and the Environment* 539–545 (Institution of Engineers Australia, 1996).
64. Eckhardt, K. How to construct recursive digital filters for baseflow separation. *Hydrol. Process.* **19**, 507–515 (2005).
65. Furey, P. R. & Gupta, V. K. A physically based filter for separating base flow from streamflow time series. *Water Resour. Res.* **37**, 2709–2722 (2001).
66. Tularam, G. A. & Ilahee, M. Exponential smoothing method of base flow separation and its impact on ontinuous loss estimates. *Am. J. Environ. Sci.* **4**, 136–144 (2008).
67. Willems, P. A time series tool to support the multi-criteria performance evaluation of rainfall-runoff models. *Environ. Model. Softw.* **24**, 311–321 (2009).
68. Brutsaert, W. Long-term groundwater storage trends estimated from streamflow records: climatic perspective. *Water Resour. Res.* **44**, W02409 (2008).
69. Rammal, M. et al. Technical note: an operational implementation of recursive digital filter for base flow separation. *Water Resour. Res.* **54**, 8528–8540 (2018).
70. Vogel, R. M. & Kroll, C. N. Estimation of baseflow recession constants. *Water Resour. Manage.* **10**, 303–320 (1996).
71. Cox, P. M., Huntingford, C. & Williamson, M. S. Emergent constraint on equilibrium climate sensitivity from global temperature variability. *Nature* **553**, 319–322 (2018).
72. Sanderson, B. M. et al. The potential for structural errors in emergent constraints. *Earth Syst. Dyn.* **12**, 899–918 (2021).
73. Chen, T. & Guestrin, C. XGBoost: a scalable tree boosting system. In *Proc. 22nd ACM SIGKDD International Conference on Knowledge Discovery and Data Mining* (eds Krishnapuram, B. et al.) 785–794 (Association for Computing Machinery, 2016); https://doi.org/10.1145/2939672.2939785
74. Gupta, H. V., Kling, H., Yilmaz, K. K. & Martinez, G. F. Decomposition of the mean squared error and NSE performance criteria: implications for improving hydrological modelling. *J. Hydrol.* **377**, 80–91 (2009).
75. Lundberg, S. M. & Lee, S.-I. In *Proc. 31st International Conference on Neural Information Processing Systems* (Ulrike von Luxburg, U. et al.) 4768–4777 (Curran Associates, 2017).
76. Chagas, V. B. P. et al. CAMELS-BR: hydrometeorological time series and landscape attribues for 897 catchments in Brazil—link to files. *Zenodo* https://doi.org/10.5281/zenodo.3709337 (2020).
77. Ghiggi, G. et al. G-RUN ENSEMBLE. *figshare* https://doi.org/10.6084/m9.figshare.12794075 (2021).
78. Chen, N., Yu, K., Jia, R., Teng, J. & Zhao, C. Biocrust as one of multiple stable states in global drylands. *Sci. Adv.* **6**, eaay3763 (2020).
79. Beck, H. E. et al. Present and future Köppen–Geiger climate classification maps at 1 km resolution. *Sci. Data* **5**, 180214 (2018).
80. Koirala, S., Yeh, P. J.-F., Hirabayashi, Y., Kanae, S. & Oki, T. Global-scale land surface hydrologic modeling with the representation of water table dynamics. *J. Geophys. Res. Atmos.* **119**, 75–89 (2014).
81. Müller Schmied, H. et al. The global water resources and use model WaterGAP v2.2d: model description and evaluation. *Geosci. Model Dev.* **14**, 1037–1079 (2021).

82. Sutanudjaja, E. H. et al. PCR-GLOBWB 2: a 5 arcmin global hydrological and water resources model. *Geosci. Model Dev.* **11**, 2429–2453 (2018).
83. Lvovich, M. I. World water resources, present and future. *GeoJournal* **3**, 423–433 (1979).
84. Döll, P. & Fiedler, K. Global-scale modeling of groundwater recharge. *Hydrol. Earth Syst. Sci.* **12**, 863–885 (2008).
85. Wada, Y. et al. Global depletion of groundwater resources. *Geophys. Res. Lett.* **37**, L20402 (2010).
86. Muñoz-Sabater, J. et al. ERA5-Land: a state-of-the-art global reanalysis dataset for land applications. *Earth Syst. Sci. Data* **13**, 4349–4383 (2021).
87. Walsh, R. P. D. & Lawler, D. M. Rainfall seasonality: description, spatial patterns and change through time. *Weather* **36**, 201–208 (1981).
88. Allen, R. G., Pereira, L. S., Raes, D. & Smith, M. *Crop Evapotranspiration—Guidelines for Computing Crop Water Requirements* (FAO, 1998).
89. Milly, P. C. D. & Dunne, K. A. Potential evapotranspiration and continental drying. *Nat. Clim. Change* **6**, 946–949 (2016).
90. Boussetta, S., Balsamo, G., Beljaars, A., Kral, T. & Jarlan, L. Impact of a satellite-derived leaf area index monthly climatology in a global numerical weather prediction model. *Int. J. Remote Sens.* **34**, 3520–3542 (2013).
91. Yamazaki, D. et al. A high-accuracy map of global terrain elevations. *Geophys. Res. Lett.* **44**, 5844–5853 (2017).
92. Amatulli, G., McInerney, D., Sethi, T., Strobl, P. & Domisch, S. Geomorpho90m, empirical evaluation and accuracy assessment of global high-resolution geomorphometric layers. *Sci. Data* **7**, 162 (2020).
93. Poggio, L. et al. SoilGrids 2.0: producing soil information for the globe with quantified spatial uncertainty. *SOIL* **7**, 217–240 (2021).
94. Huscroft, J., Gleeson, T., Hartmann, J. & Börker, J. Compiling and mapping global permeability of the unconsolidated and consolidated Earth: GLobal HYdrogeology MaPS 2.0 (GLHYMPS 2.0). *Geophys. Res. Lett.* **45**, 1897–1904 (2018).
95. Shangguan, W., Hengl, T., Jesus de, J. M., Yuan, H. & Dai, Y. Mapping the global depth to bedrock for land surface modeling. *J. Adv. Model. Earth Syst.* **9**, 65–88 (2017).
96. Hengl, T. et al. SoilGrids250m: global gridded soil information based on machine learning. *PLoS ONE* **12**, e0169748 (2017).

## Acknowledgements

This work received support from the National Key Research and Development Program of China (grant no. 2023YFC3206600 to X.L.) and the National Natural Science Foundation of China (grant no. 41922050 to X.L.).

## Author contributions

J.X. conceived this study, performed all calculations and wrote initial drafts of the manuscript. X.L. supervised the study and frequently discussed the results. S.J. and W.R.B. provided critical insights into the data analysis and made major contributions to text revisions. K.W. and C.L. contributed to streamflow data collection. M.R., M.J. and S.K. provided substantial input into data interpretation and method validation, leading to a more robust assessment. All authors discussed the results and edited the manuscript.

## Competing interests

The authors declare no competing interests.

## Additional information

**Extended data** is available for this paper at https://doi.org/10.1038/s41561-024-01483-5.

**Correspondence and requests for materials** should be addressed to Xiaomang Liu.

**Peer review information** *Nature Geoscience* thanks Arik Tashie and Hamidreza Mosaffa for their contribution to the peer review of this work. Primary Handling Editor: Tom Richardson, in collaboration with the *Nature Geoscience* team.

https://doi.org/10.1038/s41561-024-01483-5

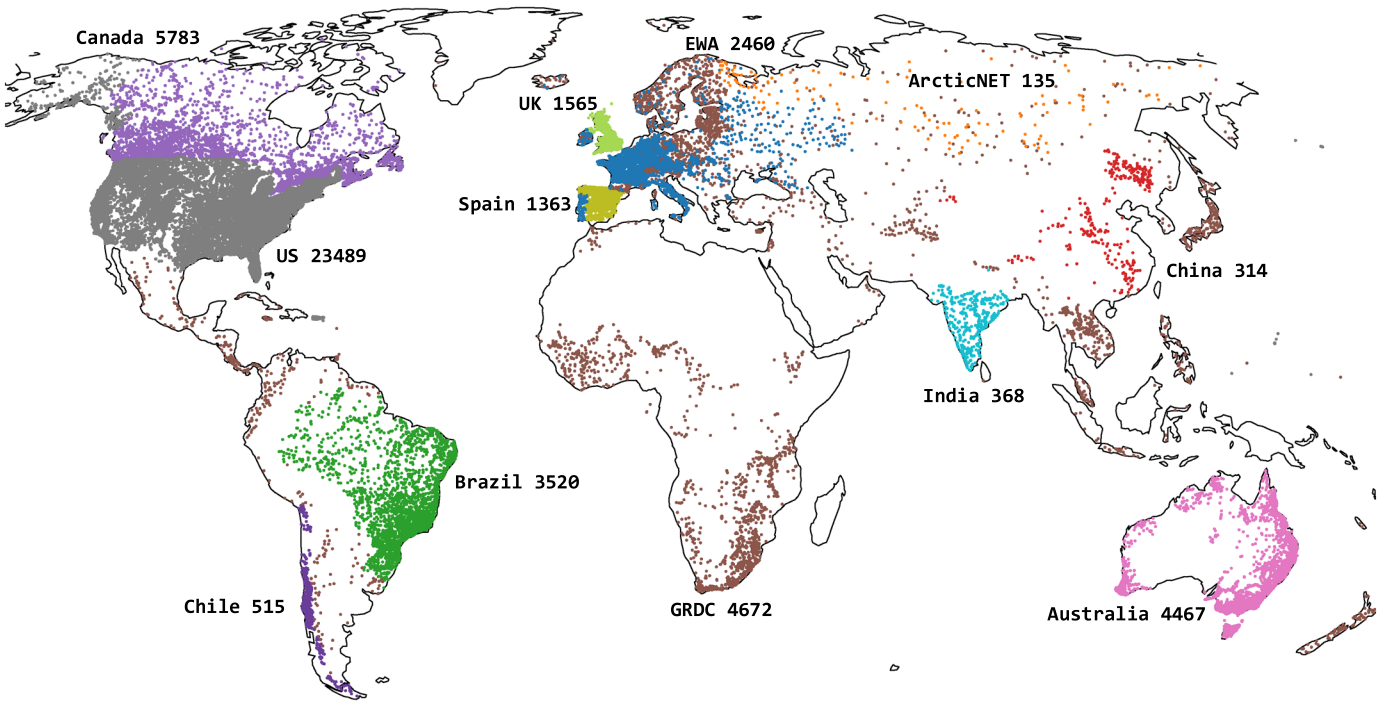


**Extended Data Fig. 1 | Compile of daily streamflow observations for 48,651 basins from 9 national agencies and 3 research databases.** The 9 national agencies are labeled in the Figure, and the three research databases are Network for the Arctic Region (ArcticNET), European Water Archive (EWA), and Global Runoff Data Centre (GRDC). We eliminated duplicates in the three research databases using the procedures outlined in Gudmundsson & Seneviratne[45]. The 48,651 basin boundaries were delineated using an automatic outlet relocation method[46]. Daily streamflow observations were downloaded in February 2023 from the links listed in the Acknowledgments.

https://doi.org/10.1038/s41561-024-01483-5

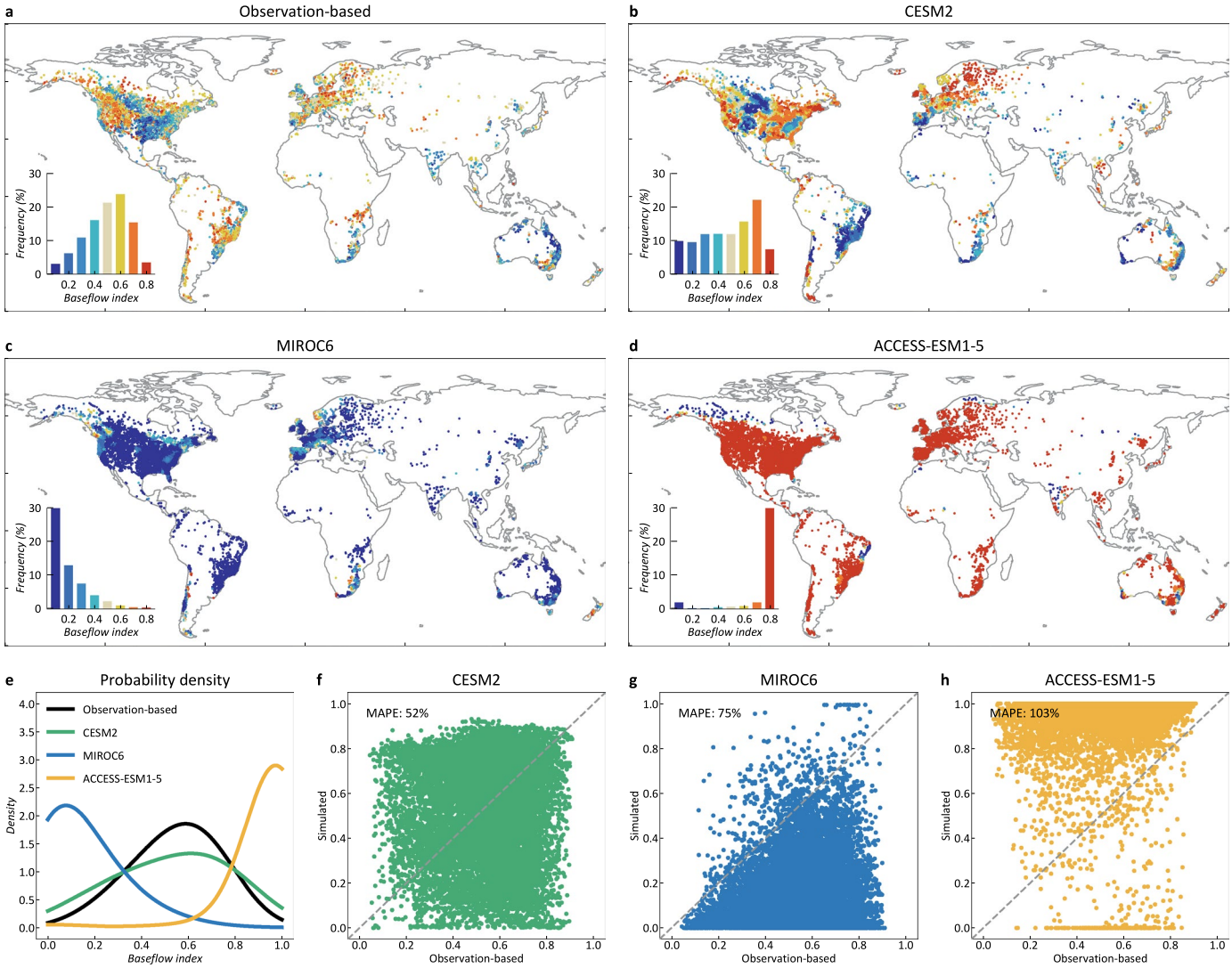


**Extended Data Fig. 2 | Simulated baseflow index for three ESMs in 15,496 small basins.** (**a**) baseflow indices calculated from daily streamflow observations using an average of 12 baseflow separation methods. (**b**–**d**) baseflow indices extracted from (**b**) CESM2, (**c**) MIROC, and (**d**) ACCESS-ESM1-5. (**e**) Probability density distribution of the 15,496 baseflow indices. (**f**–**h**) Scatter plots comparing the observation-based baseflow indices with those from (**f**) CESM2, (**g**) MIROC6, and (**h**) ACCESS-ESM1-5. MAPE stands for mean absolute percentage error.

https://doi.org/10.1038/s41561-024-01483-5

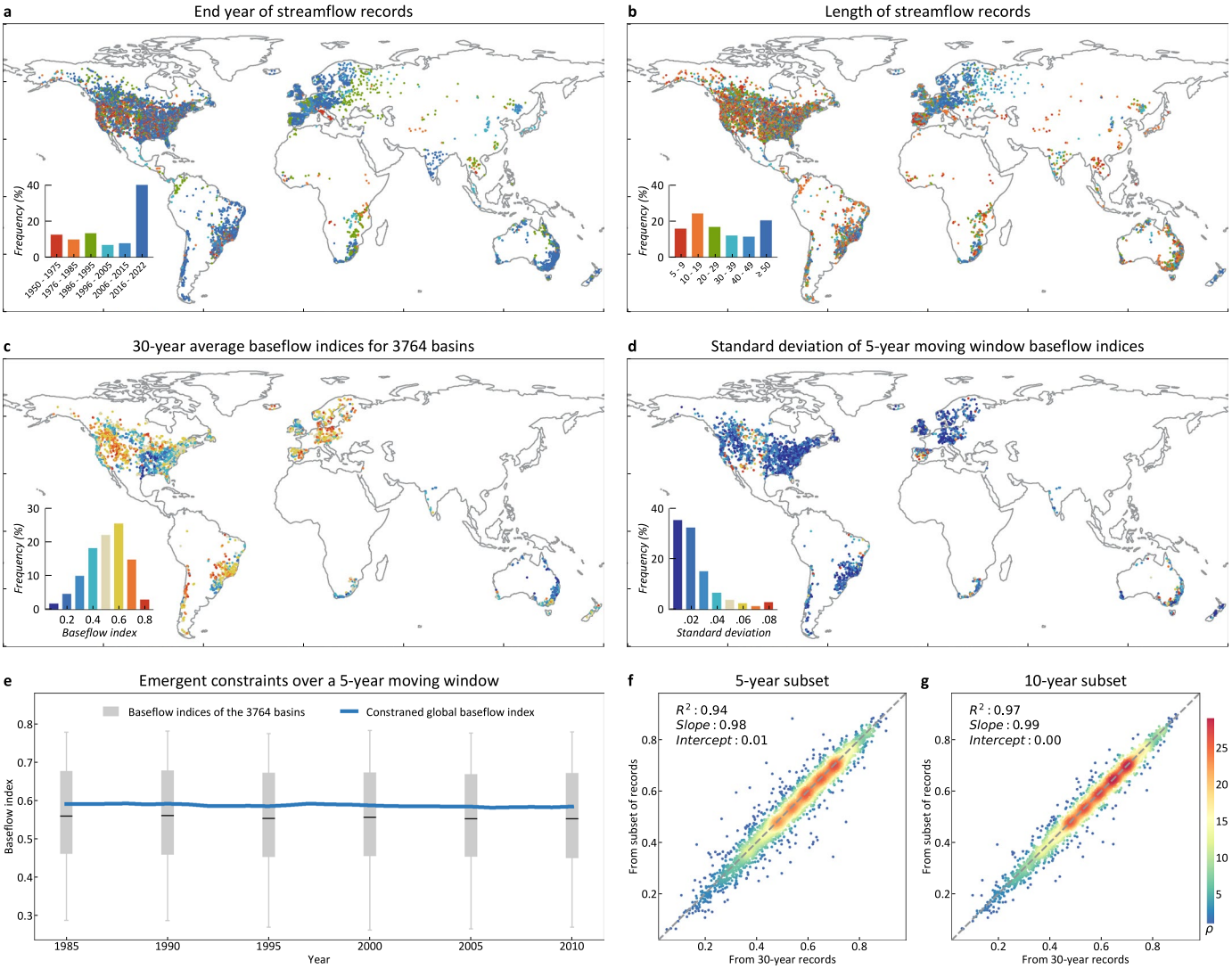


**Extended Data Fig. 3 | Temporal coverage of streamflow records.** (**a**) End year of streamflow records. The legend, which indicates the percentages of basin numbers, has been truncated below 40% to enhance readability. The blue bar reveals that streamflow records for 51% of the basins ended between 2016 and 2022. (**b**) Duration of streamflow records. 84% of the basins have streamflow records of at least 10 years. (**c**) Baseflow indices of 3,764 basins that have complete streamflow records for the 30 years from 1985 to 2014. We selected the period from 1985 to 2014 because this 30-year period has the largest number of basins with complete records. The spatial standard deviation of the 3,764 baseflow indices is 0.15. (**d**) Temporal standard deviation of baseflow indices. We performed baseflow separation methods over a 5-year moving window from 1985 to 2014, resulting in 26 baseflow indices for each basin. The standard deviation of the 26 baseflow indices was calculated to indicate decadal temporal variability. 68% of basins have a temporal standard deviation of less than 0.03, considerably smaller than the spatial standard deviation of 0.15. (**e**) We applied emergent constraints over a 5-year moving window across the 3,764 basins, resulting in 26 constrained global baseflow indices. The 26 constraints, depicted by the blue line, remain stable within the range of 0.58 to 0.59, demonstrating the stationarity of the emergent constraint approach. The grey boxes represent baseflow indices of the 3,764 basins in the given year displayed on the x-axis. The horizontal line within each box represents the mean baseflow index estimates, and the box lengths encompass the first to third quartiles. The whiskers of the boxes do not exceed 1.5 times the box lengths. (**f**) Density scatter plot of 30-year versus 5-year (1985–1989) baseflow indices. The slope of 0.98 and intercept of 0.01 suggest that 5-year streamflow records can well capture the global spatial variations of baseflow indices. The $R^2$ value of 0.94 ($p < 0.001$) demonstrates that 5-year baseflow indices can well represent long-term baseflow indices, despite some discreteness introduced by temporal variability. (**g**) Density scatter plot of 30-year versus 10-year (1985–1994) baseflow indices. The x-axis represents the 30-year baseflow indices of the 3,764 basins between 1985 and 2014. The $R^2$ value of 0.97 also has a p-value less than 0.001. All p-values in this study were derived from two-sided correlation tests, which check if the correlation is significantly different from zero based on the t-distribution, without adjusting for multiple comparisons.

https://doi.org/10.1038/s41561-024-01483-5

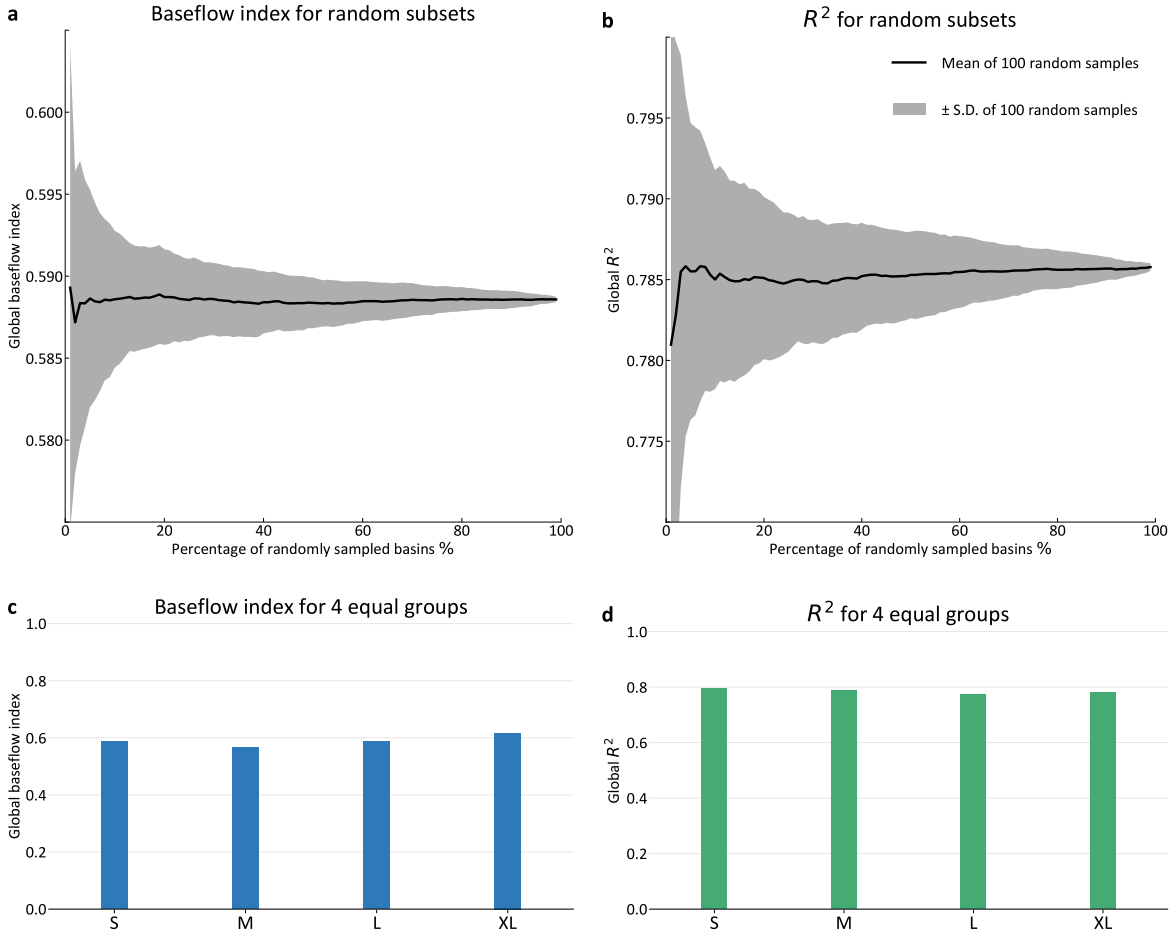


**Extended Data Fig. 4 | Sensitivity of the constrained global (a) baseflow index and (b) $R^2$ in response to the number of basins.** The x-axis represents the percentage of basins randomly sampled from a total of 15,496 basins. For each percentage, we performed random sampling and applied the emergent constraint approach in 100 iterations. The black line indicates the average constrained results obtained from the 100 iterations, and the grey shadow depicts the standard deviation across the iterations. The results demonstrate that the constrained global baseflow index remains stable at 59%, and the $R^2$ of emergent constraint remains stable at 0.79, even when utilizing only 20% of the available basins. Constrained global (**c**) baseflow index and (**d**) $R^2$ for different basin area groups. We used quartiles of basin areas to divide the 15,496 basins into four equal groups, namely small, medium, large, and extra large. The constrained baseflow index for these four groups ranges from 57% to 62%, and $R^2$ ranges from 0.77 to 0.79. All groups yield a global baseflow index close to 59%, demonstrating that scaling from basins to grid cells may be a random error.

https://doi.org/10.1038/s41561-024-01483-5

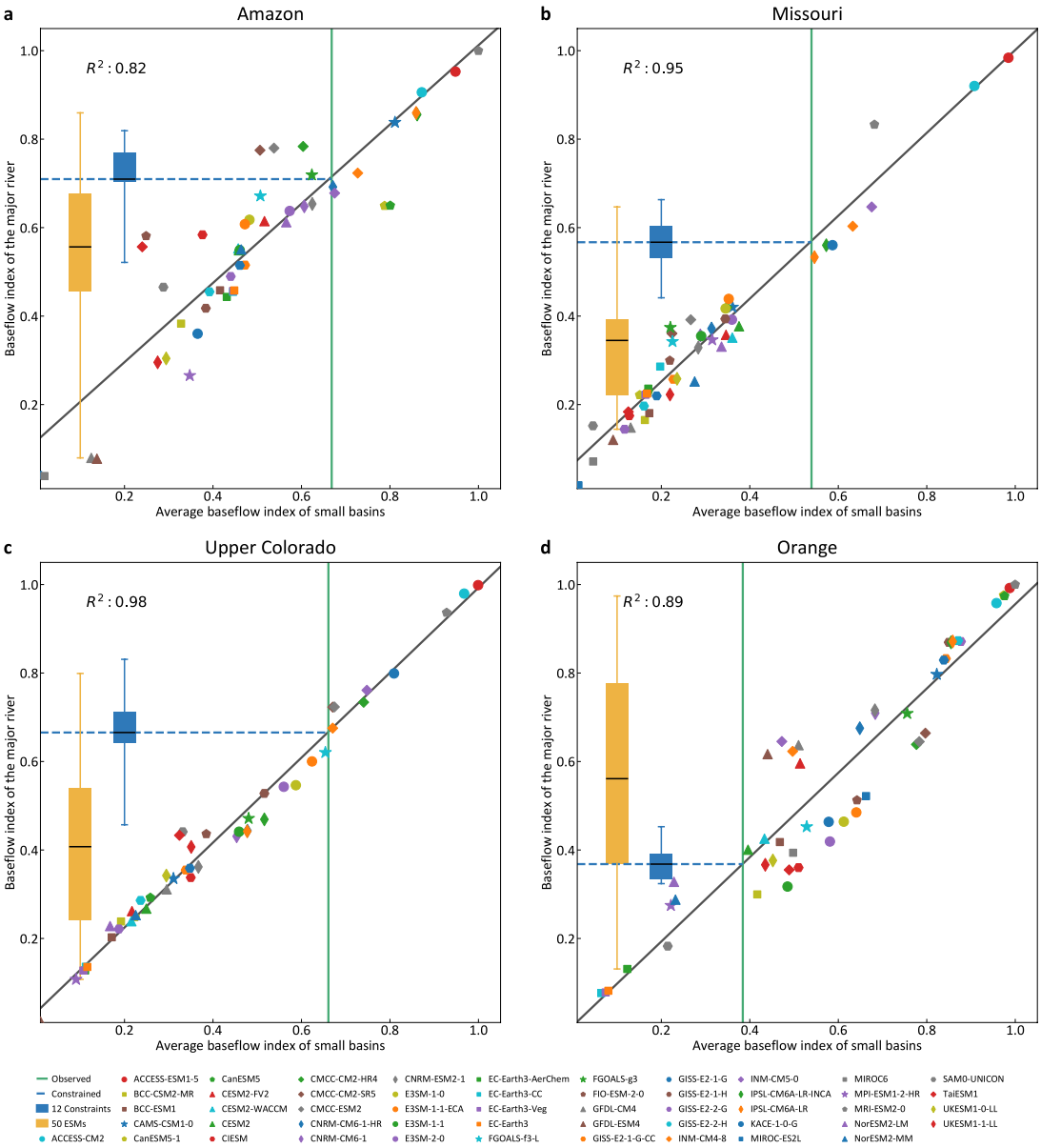


**Extended Data Fig. 5 | Emergent constraints in four major rivers.** (**a**) The Amazon River. (**b**) The Missouri River. (**c**) The Upper Colorado River. (**d**) The Orange River. Each scatter represents an ESM. For a specific ESM, the x-axis represents its simulated mean baseflow index across small basins in the major river, while the y-axis represents the global baseflow index. The black regression line depicts the relationship between the x- and y-axis variables for the 50 ESMs. All four regressions exhibit an $R^2 > 0.8$ with $p < 0.001$. The vertical green line corresponds to the observation-based mean baseflow index across the small basins within the major river, calculated as an average from 12 baseflow separation methods. The horizontal blue dotted line indicates the new baseflow index estimate of the major river through emergent constraint. The blue box represents 12 constrained baseflow index estimates of the major river, which are derived by substituting 12 vertical green lines (not shown) from different baseflow separation methods into the regression relationship. The yellow box represents 50 global baseflow index estimates from the ESMs. The horizontal line within each box represents the mean baseflow index estimates, and the box lengths encompass the first to third quartiles. The whiskers of the boxes do not exceed 1.5 times the box lengths. Outliers beyond the whiskers are not displayed here. The first three rivers have tracer-based baseflow indices of 70%, 57%, and 56%, respectively. As for the last river (Orange River), emergent constraint decreased the original value of 56% ± 26% to 37% ± 5%. The new baseflow index appears to be more plausible due to the extensive presence of biological soil crusts[78] in the Orange River.

https://doi.org/10.1038/s41561-024-01483-5

**Extended Data Table 1 | The 50 CMIP6 Earth system models used in this study and their coupled land surface models (LSM)**

| | Model | Institute | Coupled LSM | | Model | Institute | Coupled LSM |
|---|---|---|---|---|---|---|---|
| 1 | ACCESS-CM2 | CSIRO-ARCCSS | CABLE2.5 | 26 | FGOALS-f3-L | CAS | CLM4.0 |
| 2 | ACCESS-ESM1-5 | CSIRO | CABLE2.4 | 27 | FGOALS-g3 | CAS | CLM4.0 |
| 3 | BCC-CSM2-MR | BCC | BCC_AVIM2 | 28 | FIO-ESM-2-0 | FIO-QLNM | CLM4.0 |
| 4 | BCC-ESM1 | BCC | BCC_AVIM2 | 29 | GFDL-CM4 | NOAA-GFDL | GFDL-LM4.0.1 |
| 5 | CAMS-CSM1-0 | CAMS | CoLM | 30 | GFDL-ESM4 | NOAA-GFDL | GFDL-LM4.1 |
| 6 | CanESM5-1 | CCCma | CLASS3.6-CTEM1.2 | 31 | GISS-E2-1-G-CC | NASA-GISS | GISS-LSM |
| 7 | CanESM5 | CCCma | CLASS3.6-CTEM1.2 | 32 | GISS-E2-1-G | NASA-GISS | GISS-LSM |
| 8 | CESM2-FV2 | NCAR | CLM5.0 | 33 | GISS-E2-1-H | NASA-GISS | GISS-LSM |
| 9 | CESM2-WACCM | NCAR | CLM5.0 | 34 | GISS-E2-2-G | NASA-GISS | GISS-LSM |
| 10 | CESM2 | NCAR | CLM5.0 | 35 | GISS-E2-2-H | NASA-GISS | GISS-LSM |
| 11 | CIESM | THU | CIESM-LM, Modified CLM4.0 | 36 | INM-CM4-8 | INM | INM-LND1 |
| 12 | CMCC-CM2-HR4 | CMCC | CLM4.5 | 37 | INM-CM5-0 | INM | INM-LND1 |
| 13 | CMCC-CM2-SR5 | CMCC | CLM4.5 | 38 | IPSL-CM6A-LR-INCA | IPSL | ORCHIDEE v2.0 |
| 14 | CMCC-ESM2 | CMCC | CLM4.5 | 39 | IPSL-CM6A-LR | IPSL | ORCHIDEE v2.0 |
| 15 | CNRM-CM6-1-HR | CNRM-CERFACS | ISBA-CTRIP | 40 | KACE-1-0-G | NIMS-KMA | JULES-HadGEM3-GL7.1 |
| 16 | CNRM-CM6-1 | CNRM-CERFACS | ISBA-CTRIP | 41 | MIROC-ES2L | MIROC | MATSIRO6.0 |
| 17 | CNRM-ESM2-1 | CNRM-CERFACS | ISBA-CTRIP | 42 | MIROC6 | MIROC | MATSIRO6.0 |
| 18 | E3SM-1-0 | E3SM-Project | ELM v1.0 | 43 | MPI-ESM1-2-HR | MPI-M | JSBACH3.20 |
| 19 | E3SM-1-1-ECA | E3SM-Project | ELM v1.1 | 44 | MRI-ESM2-0 | MRI | HAL 1.0 and MRI-LCCM2 |
| 20 | E3SM-1-1 | E3SM-Project | ELM v1.1 | 45 | NorESM2-LM | NCC | CLM5.0 |
| 21 | E3SM-2-0 | E3SM-Project | ELM v2.0 | 46 | NorESM2-MM | NCC | CLM5.0 |
| 22 | EC-Earth3-AerChem | EC-Earth-Consortium | H-TESSEL | 47 | SAM0-UNICON | SNU | CLM4.0 |
| 23 | EC-Earth3-CC | EC-Earth-Consortium | H-TESSEL and LPJ-GUESS | 48 | TaiESM1 | AS-RCEC | CLM4.0 |
| 24 | EC-Earth3-Veg | EC-Earth-Consortium | H-TESSEL and LPJ-GUESS | 49 | UKESM1-0-LL | MOHC | JULES-HadGEM3-GL7.1 |
| 25 | EC-Earth3 | EC-Earth-Consortium | H-TESSEL | 50 | UKESM1-1-LL | MOHC | JULES-HadGEM3-GL7.1 |

https://doi.org/10.1038/s41561-024-01483-5

**Extended Data Table 2 | Emergent constraints in 17 major rivers**

| River | Lon | Lat | Area ($km^2$) | Counts | $R^2$ | CMIP6 | Constrained |
|---|---|---|---|---|---|---|---|
| Missouri | -93.52 | 39.22 | 1245413 | 794 | 0.95 | 35% ± 20% | 57% ± 7% |
| Upper Colorado | -111.59 | 36.87 | 279923 | 477 | 0.98 | 41% ± 24% | 67% ± 12% |
| Mississippi | -90.91 | 32.31 | 2937494 | 2538 | 0.93 | 51% ± 20% | 52% ± 6% |
| Columbia | -123.26 | 46.15 | 652008 | 753 | 0.99 | 62% ± 20% | 69% ± 12% |
| Yangtze | 120.23 | 31.93 | 1908183 | 13 | 0.84 | 59% ± 17% | 53% ± 4% |
| Mekong | 105.71 | 10.11 | 772720 | 38 | 0.89 | 61% ± 19% | 54% ± 6% |
| Yellow | 118.91 | 37.78 | 760638 | 16 | 0.71 | 55% ± 18% | 53% ± 3% |
| Godavari | 81.89 | 16.76 | 307890 | 10 | 0.96 | 47% ± 24% | 34% ± 3% |
| Volga | 47.99 | 46.55 | 1404425 | 21 | 0.98 | 48% ± 25% | 57% ± 9% |
| Danube | 29.06 | 45.36 | 792207 | 294 | 0.96 | 60% ± 19% | 62% ± 10% |
| Dnieper | 32.79 | 46.67 | 506894 | 21 | 0.98 | 46% ± 24% | 56% ± 10% |
| Amazon | -51.54 | -1.29 | 5886220 | 26 | 0.82 | 56% ± 22% | 71% ± 9% |
| La Plata | -58.45 | -34 | 2621720 | 362 | 0.89 | 49% ± 22% | 68% ± 8% |
| Murray-Darling | 138.97 | -35.56 | 902849 | 469 | 0.92 | 44% ± 28% | 44% ± 6% |
| Orange | 16.79 | -28.35 | 887200 | 26 | 0.89 | 56% ± 26% | 37% ± 5% |
| Zambezi | 36.32 | -18.61 | 1369680 | 73 | 0.84 | 62% ± 22% | 62% ± 7% |
| Limpopo | 33.65 | -25.02 | 403019 | 37 | 0.92 | 51% ± 25% | 52% ± 8% |

Major rivers are basins with an area larger than 250,000 $km^2$, that is, a minimum of 100 grids at the 0.5-degree resolution of CMIP6. The reason for the area limitation is that we cannot apply emergent constraints to small rivers, which may only contain a few observation-based baseflow indices. 'Counts' represent the number of observation-based baseflow indices in each river used for emergent constraint. 'CMIP6' refers to the baseflow index derived from 50 CMIP6 ESMs, expressed as the mean ± standard deviation. 'Constrained' represents the new baseflow index estimates obtained from emergent constraints.

https://doi.org/10.1038/s41561-024-01483-5

**Extended Data Table 3 | Constrained baseflow indices in different climate zones**

| Climate | Area ($km^2$) | Counts | $R^2$ | CMIP6 | Constrained |
|---|---|---|---|---|---|
| Tropical | 32529908 | 1155 | 0.75 | 58% ± 21% | 67% ± 7% |
| Arid | 51738185 | 2076 | 0.77 | 50% ± 19% | 61% ± 6% |
| Temperate | 15739219 | 7806 | 0.72 | 62% ± 17% | 56% ± 5% |
| Continental | 24485708 | 4415 | 0.61 | 52% ± 18% | 61% ± 8% |

Based on the Köppen-Geiger climate classification[79], we established emergent constraint relationships for different climate zones using their internal small basins. Polar climate zones are not included in this table due to insufficient data coverage. 'Counts' represent the number of observation-based baseflow indices in each climate zone used for emergent constraint. 'CMIP6' refers to the baseflow index derived from 50 CMIP6 ESMs, expressed as the mean±standard deviation. 'Constrained' represents the new baseflow index estimates obtained from emergent constraints.

https://doi.org/10.1038/s41561-024-01483-5

**Extended Data Table 4 | Previous global groundwater recharge statistics**

| Reference | Method | Recharge ($10^3$ km$^3$ yr$^{-1}$) | Runoff ($10^3$ km$^3$ yr$^{-1}$) | Recharge/ Runoff | Precipitation ($10^3$ km$^3$ yr$^{-1}$) | Recharge/ Precipitation |
|---|---|---|---|---|---|---|
| Lvovich (1979)[83] | Baseflow analysis | 12 | 38.3 | 31% | 110.3 | 11% |
| Döll & Fiedler (2008)[84] | WaterGAP 2.1f | 12.7 | 39.4 | 32% | 104.7 | 12% |
| Wada et al. (2010)[85] | PCR-GLOBWB | 15.2 | 36.2 | 42% | 95.5 | 16% |
| Koirala et al. (2014)[80] | MATSIRO | 29.9 | 45.5 | 66% | 111 | 27% |
| Sutanudjaja et al. (2018)[82] | PCR-GLOBWB 2 | 25.5 | 44.0 | 58% | 107.5 | 24% |
| Müller Schmied et al. (2021)[81] | WaterGAP 2.2d | 16.4 | 40.7 | 40% | 111.6 | 15% |
| Masson-Delmotte et al. (2021)[14] | IPCC Sixth Assessment Report | 13 | 46 | 28% | 120 | 11% |
| Current | Emergent Constraint | > 21.7 | 36.8 | > 59% | 105 | > 21% |

Groundwater recharge is the sum of groundwater evapotranspiration, groundwater discharged into rivers (baseflow), subsurface seepage out of the basin, and changes in groundwater storage[31]. Hence the constrained global baseflow index of 59% represents the lower bound for the long-term ratio between groundwater recharge and total runoff. Precipitation and total runoff for this study were obtained by averaging the three G-RUN ENSEMBLE members driven by the Climatic Research Unit, Global Soil Wetness Project Phase 3, and Princeton Global Forcing Version 3. As shown below, a decade ago, the old versions of the WaterGAP and PCR-GLOBWB models yielded groundwater recharge ratios (that is, recharge as a proportion of precipitation) of 12% and 16%. Subsequently, Koirala et al.[80] suggested that these two recharge ratio estimates were underestimated, and integrated water table dynamics into the MATSIRO land surface model, resulting in a higher recharge ratio of 27%. In recent versions of WaterGAP and PCR-GLOBWB, the recharge ratio estimates were increased to 15% and 24%, respectively. The increase in WaterGAP's estimate may be attributed to the introduction of focused groundwater recharge[81] (infiltration from surface water bodies such as lakes and wetlands), whereas for PCR-GLOBWB it is likely due to a better representation of spatial heterogeneity such as aquifer transmissivity[44,82]. The first three rows were sourced from refs. 83–85. All statistics are performed excluding Greenland and Antarctica, except for the IPCC Sixth Assessment Report, which includes these regions. Additionally, our observational constraint further excludes regions with continuous permafrost.

https://doi.org/10.1038/s41561-024-01483-5

**Extended Data Table 5 | Environmental drivers used as training data for baseflow index simulation**

| Type | Name | Description | CMIP6 | Units | Calculation |
|---|---|---|---|---|---|
| Water | P | Precipitation | pr | mm $yr^{-1}$ | Annual average of total precipitation for ERA5-Land[86] |
| | Snow | Snowfall | prsn | mm $yr^{-1}$ | Annual average of snowfall for ERA5-Land |
| Seasonality | SI | Seasonality Index | pr | unitless | Calculated according to Walsh & Lawler[87]: $$SI = \frac{1}{P}\sum_{n=1}^{12}\left\lvert x_n - \frac{P}{12}\right\rvert$$ where $P$ is the annual mean precipitation, $x_n$ is the mean precipitation of month $n$ |
| Energy | T | 2m Temperature | tas | K | Derived from ERA5-Land monthly aggregated data |
| | Rn | Surface Net Radiation | rsds, rlds, rsus, rlus | W $m^{-2}$ | The sum of net solar radiation and net thermal radiation for ERA5-Land. For CMIP6 we use: $$R_n = (rsds + rlds) - (rsus + rlus)$$ |
| | VPD | Vapor Pressure Deficit | huss, ps, tas | kPa | Calculated from the 2m dewpoint temperature of ERA5-Land based on equation 14 in Allen et al.[88]. For CMIP6 we followed equation 18 in Milly & Dunne[89] |
| | Wind | 10m Wind Speed | sfcWind | m $s^{-1}$ | Calculated from eastward and northward components of 10m wind for ERA5-Land |
| Vegetation | LAI | Leaf Area Index | lai | unitless | Calculated from low and high vegetation LAI of ERA5-Land based on equation 12 in Boussetta et al.[90] |
| Topography | ELEV | Elevation | | m | A digital elevation model from Yamazaki et al.[91] |
| | Slope | Slope | | degree | Calculated from the above digital elevation model |
| | TWI | Topographic Wetness Index | | ln $m^2$ | Download from the Geomorpho90m[92] dataset. Calculated as $\ln\frac{a}{\tan b}$, where $a$ is the upstream contributing area and $b$ is the local slope |
| Soil | ρb | Bulk Density | | cg $cm^{-3}$ | Depth-weighted bulk density for 6 depth intervals within 0-200cm from SoilGrids 2.0[93] |
| | Perm | Permeability | | $\log_{10}$ $m^2$ | Logarithmic permeability from global hydrogeology maps v2.0[94] |
| | Frag | Coarse Fragment | | volume % | SoilGrids 2.0 depth-weighted volumetric content of fragments larger than 2 mm |
| | Sand | Sand Content | | weight % | SoilGrids 2.0 depth-weighted sand content |
| | Silt | Silt Content | | weight % | SoilGrids 2.0 depth-weighted silt content |
| | Clay | Clay Content | | weight % | SoilGrids 2.0 depth-weighted clay content |
| Bedrock | DTB | Depth to Bedrock | | cm | Bedrock depth map from Shangguan et al.[95,96] |

Environmental drivers were sourced from refs. 86–96